UNIVERSITÀ DEGLI STUDI DI MILANO

PHD COURSE IN CLINICAL RESEARCH, XXXV CYCLE

Department of Biomedical, Surgical and Dental Sciences

PhD Thesis

The digital nose: computational fluid dynamics as a new tool for the assessment of physiological, pathological and virtual post-surgical nasal air flow

PhD Student

Antonio Mario BULFAMANTE

Matr. R12687

Tutor

Prof. Carlotta PIPOLO

Coordinator

Prof. Massimo DEL FABBRO

Academic Year 2021 – 2022

Summary

1. Introduction

Nasal stenosis is the most common symptom of a variety of nasal pathologies. In a large study of 4,611 patients with rhinosinusitis, 66 percent of patients exhibited nasal stenosis [1]. In a separate study, it was found in 70% of 755 patients [2]. Several conditions, including rhinosinusitis, nasal septal deviation, concha bullosa (middle turbinate pneumatization), and turbinate hypertrophy, can cause nasal obstruction. All of these factors are prevalent among the general population. For instance, the prevalence of nasal septal deviation in the general population ranges from 9.5% in children to 19.4% in adults [3], and in the study by Smith et al analyzing 883 CT scans, 67.5% of patients exhibited pneumatization of at least one concha [4]. If medical treatment fails to alleviate nasal obstruction, surgery may be the only option, but the surgical plan is largely dependent on the surgeon's experience. Existing methods for assessing nasal flow are inaccurate and unable to determine which of the singles considered anatomical abnormalities has the greatest impact on nasal flow modification. Consequently, it should be addressed with greater vigour during surgery. This lack of information leads to the performance of numerous procedures for which we have, at best, only anecdotal evidence of additional success, but which unquestionably prolong surgical time, which has a direct effect on the number of hours spent in the operating room, potential complications, and costs. Our research aims to examine the application of a new tool, Computational Fluid Dynamics (CFD), in a variety of clinical settings. CFD is the branch of Fluids Mechanics that studies the behaviour of fluids in their environments and in relation to solids. In otorhinolaryngology, for instance, CFD can be utilized to examine airflow in the nose or upper airways. Our multidisciplinary team believes that in the future, CFD could be used on a daily basis, moving from the research field to the clinical field. In this thesis, I would like to demonstrate how CFD works and how it can be applied to the study of nasal airflow, both physiologically, pathologically, and surgically. All the

examples are performed on actual CT scans, simulating realistic respiratory conditions, with the future goal of bringing CFD from the computer to the patient's bed.

2. Background

The nose is an anatomical structure with multiple functions, including respiration, temperature regulation, filtration, defence, olfactory perception, and facial aesthetics [5]. Respiration is one of the primary functions, exerting a significant influence on the others. Respiration alteration will have significant consequences, including abnormal air conditioning and filtering, secretions stasis, deterioration of sleep quality, and abnormal development of maxillofacial bones during growth [5, 6]. Reduction of nasal respiration, or, more precisely, nasal air flow, is referred to as respiratory nasal stenosis and is the primary symptom of numerous nasal pathologies. In a large study of 4,611 patients with rhinosinusitis, 66 percent of patients exhibited nasal stenosis [1]. 70 percent of 755 patients in another study had nasal stenosis, which may be caused by an alteration of nasal osteo-cartilaginous structures (e.g. nasal septal deviation, nasal bones dysmorphism, congenital malformation, etc.), an increase in the size of nasal structures (e.g. turbinate hypertrophy), or the presence of neoformations occupying the nasal air space (inflammatory or oncological diseases). Most of these causes are widespread in the general population: for instance, nasal septal deviation prevalence ranges from 9.5% in children to 19.4% in adults [3] and Smith et al. reviews of 883 CT scans revealed that 67.5 percent of patients exhibited pneumatization of at least one concha [4]. In the case of inflammatory (e.g. nasal polyposis) or oncological (e.g. inverted papilloma, nasal carcinoma, etc.) disease, the goal is to remove as much of the disease as possible. In these situations, it is permissible to adopt a more aggressive stance, even if it means sacrificing anatomical structures, and functional repercussions may be better tolerated in the name of surgical radicalism [8]. In other cases, the problem is the functional alteration, and the surgeon must improve nasal respiration, possibly for an extended period of time. To do so, the surgeon must

modify the shape, size, or position of the nasal anatomical structures [8,9]. These types of modification must be handled with care, as an overly aggressive approach could result in serious, even debilitating side effects for the patient, such as nose dysmorphism, nasal septal perforation, osteonecrosis and osteomyelitis, or empty nose syndrome (ENS) [10–12]. Specifically, ENS is a pathological condition characterized by the unpleasant sensation of nasal obstruction, inadequate nasal airflow, and lack of breath perception, despite the presence of valid and visible respiratory space. Patients frequently report an abundance of nasal crusts, nasal dryness, and occasionally pain that is only marginally responsive to painkillers [11,12]. ENS frequently causes psychological issues: the patient is completely preoccupied with nasal respiration and cannot concentrate on anything else (aprosexia nasalis). The vast majority develop major depressive disorder [13, 14]. Therefore, the surgeon acts based on his or her personal experience and attempts to adapt his or her actions on a case-by-case basis, despite the lack of objective data that can indicate how to proceed.

Throughout the years, numerous instruments and tests have been developed to aid surgeons in this intricate matter. Active anterior rhinomanometry (RMM) and the SinoNasal Outcome Test 22 (SNOT-22) are presently regarded as the gold standard. RMM is the most prevalent method for measuring nasal patency [15]. During spontaneous respiration, simultaneous measurements of trans-nasal pressure differences and nasal airflow are made on each side. Continuous evaluation of the dynamic changes in airway resistance during respiration. Frequently, the nasal airflow at a trans-nasal pressure difference of 150 Pa is reported to obtain a single outcome value. This pressure difference reflects conditions at low physical exertion, provides information on nasal resistance when mixed laminar and turbulent flow predominates, and can be attained by even the most frail patients. Mucosal decongestion with [alpha]-imidazoles may assist in distinguishing between mucosal congestion and skeletal

abnormalities. Following mucosal decongestion, mean flow increases by between 20 and 40 percent. SNOT-22 is a simple-to-use questionnaire consisting of 22 questions regarding possible symptoms associated with chronic rhinosinusitis. Each question receives a score between 0 and 5, with 0 representing the absence of the condition and 5 representing its worst possible manifestation. High total scores indicate a low standard of living (QoL). According to the 2020 European Position Paper on Rhinosinusitis and Nasal Polyps (EPOS), SNOT-22 is an effective tool for assessing the quality of life (QOL) of CRS patients [17]. RMM and SNOT-22 are valuable tools, but their results are frequently imprecise and subject to subjective interpretation [18,19]. In addition, both RMM and SNOT-22 can provide information on nasal obstruction and QoL prior to and after surgery, but neither can assist with surgical planning. Computational Fluid Dynamics (CFD), the branch of Fluids Mechanics that deals with the numerical resolution of differential Navier-Stokes equations, which govern fluid flow and make up the Navier-Stokes System [20], could provide surgeons and patients with a new possible support today. The Navier-Stokes equations are so complicated that there is no practical analytical solution, but they can be solved using numerical approximation. The Finite Volume Method is one of the most widespread procedures (FVM). Following this method, the computational domain is discretized into a finite number of cells (computational grid), and the numerical solution is obtained and advanced element-by-element in time. Three of the most common methods for capturing turbulence's effects are as follows:

RANS (Reynolds Averaged Navier-Stokes)

LES (Large Eddy Simulation)

DNS (Direct Numerical Simulation)

In accordance with the RANS method, turbulence effects are indirectly accounted for via a model of turbulence designed for high-speed aerospace and industrial applications. In rhinology, however, flows are typically characterized by slow speeds. In addition, to solve the equations using this method, a turbulence model that recovers the information lost due to the mean operator is required. Sadly, these turbulence models are empirically calibrated, thereby introducing the so-called model error. Importantly, all numerical methods introduce an error into the solution due to the discretization process, whereas the error introduced by the turbulence model is typically uncontrollable, a priori, and of many orders of magnitude. In addition, as a result of the mean operator, the solution of the Navier-Stokes mediated equations is no longer composed of the instantaneous velocity and pressure fields, but rather their respective time means. This indicates that this solution is incapable of describing unsteady flows (such as nasal air flow) because the time variable is lost in the process. RANS is problematic for non-normal anatomy, such as nasal anatomy.

In contrast, the Navier–Stokes equations are numerically solved without any turbulence model in the DNS approach. This implies that the computational mesh must resolve the entire range of spatial and temporal scales of the turbulence, from the smallest dissipative scales (Kolmogorov microscales) up to the integral scale, associated with the motions containing the majority of the kinetic energy. LES is positioned between RANS and DNS, providing a more accurate solution than RANS while avoiding the prohibitive computational cost of DNS. LES restricts the application of turbulence modelling to the resolution of small turbulence scales via a filtering operation. The filtering operation is closely related to the computational grid, and it is possible to roughly control the amount of turbulence that is calculated and modelled. In other words, it is possible to tailor the solution's quality [21].

Once a model has been created, it can be used to simulate multiple flow characteristics simultaneously, and the same model provides access to different quantities, such as pressure variation through the various nose parts, flow rate, temperature changes, turbulence, etc., as shown in Fig. 1.

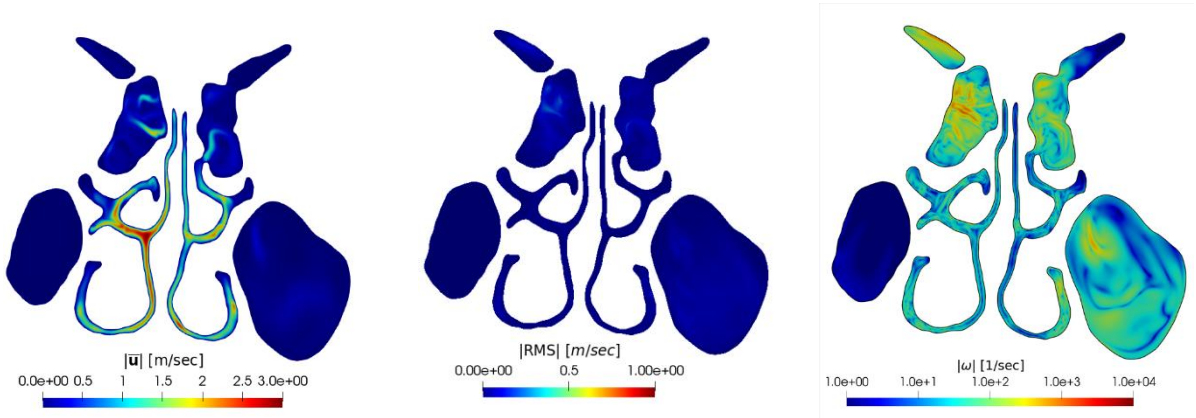

Figure 1 Different flow characteristic have been simulated and analyzed in the same virtual model. a) Flow velocity in both nasal fossae and paranasal sinuses. b) Root mean square of flow velocity . c) Vorticity magnitude, to analyze vorticity.

LES and DNS are not yet routinely employed in computational studies of the nasal airflow, despite their widespread use in the CFD community for many applied problems. Due to the low computational demand and lack of adequate technological support, the majority of groups opted to use RANS methods. However, we are confident that DNS and LES will produce superior results compared to RANS. In addition, the anatomical details of the frontal and maxillary sinuses are frequently omitted from the existing examples [22–24], despite their significance in the treatment of numerous disorders. We have decided to employ realistic models, thereby increasing computational requirements once more. We collaborated with the Department of Aerospace Science and Technologies (DAER) at Politecnico di Milano to make all of this possible. Supercomputers at the CINECA Supercomputing Center (Bologna, Italy) performed all of the calculations. We believe that high quality results will make CFD a potent tool in the process of patient-tailored surgery, enabling the "computer-to-bed" step. In

addition, it can measure normal or altered flow [18–24] and it permits the investigation of a variety of situations and conditions, such as the physiological distribution of nasal flow and, consequently, of the particles or gases carried by nasal flow. For instance, it can simulate the distribution of a nasal topical drug by predicting its distribution based on the weight of its constituent particles. From our perspective, CFD is a tool with an infinite number of possible applications.

The key to making CFDs usable and widespread in the near future is their ease of use, which points to the complete automation of procedures. To achieve this objective, numerous data are required. Therefore, large databases are required to collect this information. In this vein, our multidisciplinary team designed the OpenNose project, which aims to develop a patient-specific open source workflow for the diagnosis and investigation of nasal conditions. All CT scans used in the presented studies have been obtained from this database, and all obtained results have been uploaded. OpenNose utilizes open-source software and adheres to the Open Science Guidelines. According to how scientific results are obtained, procedures and anatomical data will be made available for download by the public, albeit with appropriate anonymization and authorization. The project is not intended to be unilateral or unilinear, but it will be possible to load the results obtained by other research groups in order to stimulate comparison and establish a central exchange point for the study of the fluid dynamics of nasal flows.

3. Rationale

CFD will play a significant role in the diagnosis and therapeutic programming of ENT pathologies, whereas it is almost exclusively used in the research field at present.

In the following chapters, three applications of CFD procedures to analyze physiological, pathological, and post-virtual surgical nasal air flow will be presented. The first chapter will discuss nasal airflow distribution and water molecules as virus carriers. Modification and removal of nasal turbinates, both isolated and in conjunction with medial maxillectomy, will be discussed in the second and third chapters. There will be examples of virtual surgery and the use of CFD to simulate nasal airflow after surgery. In addition, different CFD methods will be compared in chapter two to better define inter-approach differences. In fact, in order to grant the transition "from computer to bed," it will be necessary to determine which CFD approach to employ, balancing costs (both financial and time-related) and precision of the results.

Beyond the chapter-specific objectives, which could be summarized as practical objectives, the primary objective of this thesis is to demonstrate that CFD can be transferred to the clinical field. We believe that CFD can serve as an objective diagnostic tool that enables the surgeon to treat anomalies that impair normal nasal airflow.

4. Expiratory Accumulation Of SARS-Cov-2 In The Olfactory Mucosa

Introduction

The respiratory virus SARS-CoV-2, which is still spreading rapidly throughout the world, is thought to enter an organism by way of aerosol or fomite transmission to the nose, eyes, and oropharynx[25–27]. Presentation varies from neurological symptoms like headache, dizziness, and hyposmia to respiratory symptoms like fever and cough to respiratory symptoms from the virus's target organs [27] . Access sites into the CNS and the anatomical closeness of neurons, nerve fibers, and the mucosa inside the olfactory groove are now being studied in current literature [28].· According to the observed clinical-neurological symptoms associated with changes in smell, SARS-CoV-2 may use this neuro-mucosal interface as a point of entry. Although early reports [29] support this hypothesis through autopsy sampling, There is no information on how the SARS-CoV-2 enters the mucosa at the olfactory cleft or if the involvement of the olfactory mucosa results from viral particle deposition directly or through a subsequent viral invasion of these tissues during the illness.

From other respiratory viruses, we know that aerosols, which are responsible for the transmission of airborne microorganisms, consist of small droplet nuclei (1–5µm) or droplets (>5µm) [30,31]; these have specific characteristics regarding their distribution inside the nose and respiratory tract. Considering that hyposmia more commonly follow the first signs of presentation of infection [32,33], the hypothesis of direct contact through airborne at the stage of primary infection, and therefore during inspiration, is not plausible.

The second hypothesis, which propose a subsequent spread to the olfactory groove in retrograde manner during expiration in an already challenged organism, appears more likely.

This would make CNS penetration a complication secondary to pulmonary infection, thus opening the field to so far unconsidered preventative measures.

CFD has been used to study the distribution of normal nasal airflow and deposition of supposed infectious sub-micron droplets during breathing, to better understand the possible routes of infection and penetration inside the nasal cavity and the olfactory mucosa.

Methods

Preconditions for the preparation of the 3D model

A three-dimensional model of the air volume was required to simulate biphasic flow and particle distribution simulations. In the present chapter, the air volume consisted of the nasal cavities and paranasal sinuses. For the reconstruction of this 3D model, it was necessary to start from the DICOM images of a real patient's maxillofacial CT.

CT must have some characteristics:

1. Contain all sections from the apex of the skull to the glottic plane and, anteriorly, the tip of the nose;
2. Have a spatial resolution of at least 0.5 mm x 0.5 mm in the coronal and sagittal direction;
3. Have a constant scan thickness;
4. Have a scanning thickness of 0.6 mm (maximum value 1 mm);
5. Have a spacing of the scan planes equal to the thickness of the scans;
6. Have a Gantry Tilt equal to 0°;
7. Do not use oblique scans;
8. Use a circular or square field of view (FOV);
9. Have an axial section scan.

3D models creation

For this analysis, two sets of simulations were created. The first included seven CT scans of adult patients, with normal noses or only slight nasal respiratory alterations (minimal septal deviation, paradoxical bending of the middle turbinate, Concha bullosa, etc.), without inflammatory or sinonasal neoplastic conditions. The aim was to study normal nasal air flow distribution across the nasal cavities. The second group of simulations was carried out using five CT scans to study droplets distribution through the nasal cavities. These five CT scans have been randomly selected from a database called OPEN-Nose, a multidisciplinary project born to develop an open source and patient-specific work flow for nasal condition diagnosis and study. All twelve images had previously been anonymized through a dedicated software. CT scans were performed with a 64-slice multi-detector CT scan (VCT, General Electric Healthcare, Wisconsin, USA). The CT scans featured a 512x512 matrix, with a spatial resolution of 0.49 mm in the sagittal-coronal plane, and a gap of 0.625 mm between the consecutive axial portions, with 350-400 native images for each case. Once the tomographic scans were obtained, it was necessary to transform a scale of gray values into a binary scale to allow the software to delimit the full spaces (anatomical structures) from the empty spaces (air). For this purpose, an open-source software called 3D-slicer® (Slicer.org -Ver. 4.11.20210226) [34–36] was used. 3D-slicer® allows to made this distinction semi-automatically. The operator set an electronic density value (expressed in Hounsefield Unit - HU) as a threshold, which allows to consider everything higher as "full" and everything lower as "empty"; the threshold value used for this work is -218 HU [37]. Once the space has been reconstructed, the connection between the oral cavity and the epiglottis was manually eliminated, as it was not of interest in the work presented. The edges of the model are smoothed, as more regular boundaries allowed better

division into cells (fig. 2). Each 3D-slicer® model was then finalized as a STereoLithography (STL) file.

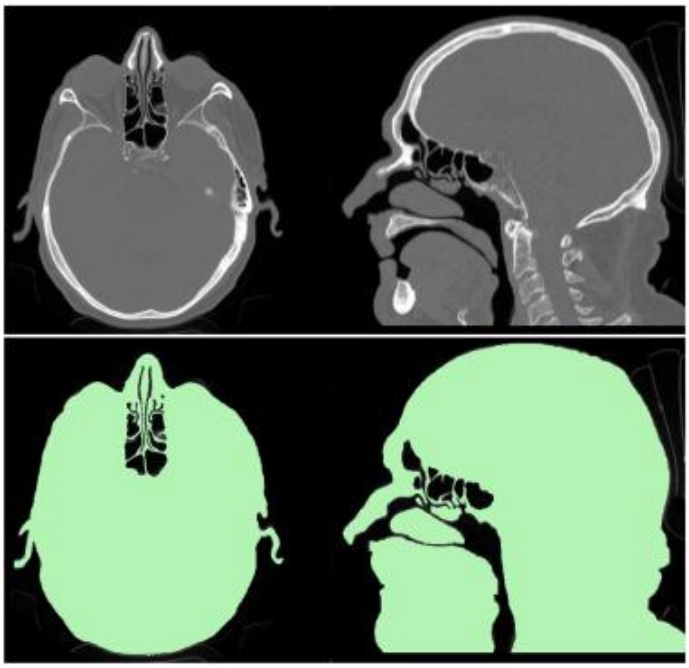

Figure 2 Example CT images (high) and their segmentation (low) obtained by setting a threshold value of HU= -281, after removal of the connection between mouth and epiglottis. Black corresponds to the aerial volume.

An external air volume complemented the model, where the droplets to be inhaled were evenly distributed at the beginning of the simulation. For this purpose, the STL anatomical surface was intersected with an external spherical volume carefully placed around the nostrils. The union of the sphere and the internal airways constituted the proper computational domain. The size and position of the sphere were designed to minimize computational overhead and simultaneously provide a high-quality mesh (fig. 3)

The model was then processed with another open-source software, called OpenFoam® (OpenCFD Ltd -Ver. v1906 / v6) [38], via the SnappyHexMesh utility to obtain the ultimate volumetric mesh.

Figure 3 Left: The entire computational domain, created by the internal airways plus the external spherical volume. Right: sagittal (blue) and coronal (red) sections, showing the volumetric mesh for the finest mesh employed in this work, made from about 25 x 10^6 cells.

Mathematical models

Air

The equations expressing the conservation of mass balance and the momentum for the continuous phase (i.e. air) are the incompressible Navier-Stokes and continuity equations:

$$\nabla \cdot u = 0 \qquad (1)$$

$$\frac{\delta u}{\delta t} + (u \cdot \nabla)u - v\nabla^2 + \frac{\nabla p}{\rho} \qquad (2)$$

where u is the velocity vector, p is the pressure, ρ is the density (constant), and ν is the kinematic viscosity. According to the LES [21] approach, the filtered form of the reference equations is used:

$$\nabla \cdot \tilde{u} = 0 \tag{3}$$

$$\frac{\delta \tilde{u}}{\delta t} + (\tilde{u} \cdot \nabla)\tilde{u} - v\nabla^2 \tilde{u} + \nabla \cdot \tau_{sgs} + \frac{\nabla p}{\rho} = 0 \tag{4}$$

Where the factorization $u = \tilde{u} + u'$ is introduced, the symbol $\tilde{}$ indicates the filtered (or resolved) component, a first indicates the subscale component (SGS) and τ_{sgs} the stress tensor of the subgrid. In the present work, emphasis was not placed on the choice of the specific model of turbulence of the subgrid. In fact, the meshes used are quite fine; as a result, the contribution of the subnet model was of modest importance, as shown below. Then τ_{sgs} was modeled through the simplest and cheapest model available, e.g. Smagorinsky's static model[39]

$$\tau_{sgs} = -2v_{sgs}\widetilde{D} \tag{5}$$

The mentioned above expression defines the tensor τ_{sgs} as proportional to the strain tensor of the filtered velocity field $\widetilde{D}$, defined as $\widetilde{D} = \frac{1}{2}(\nabla\tilde{u} + \nabla\tilde{u}^T)$, via a scalar function τ_{sgs}, the so-called subgrid of viscosity of vortices, expressed as follows:

$$v_{sgs} = l_s^2\tilde{s} = (C_s\Delta)^2\tilde{s} \tag{6}$$

in which $\tilde{s}$ is the characteristic velocity of filtered deformation, $\tilde{s} = (2\widetilde{D} : \widetilde{D})^{1/2}$and ℓs Smagorinsky length scale, assumed as proportional by the Smagorinsky coefficient $C_s \approx 0.17$ to the width of the filter Δ. This quantity is a length scale associated with the size of the computational grid and it is defined as Δ= (Δx Δy Δz) 1/3, where Δx, Δy, Δz is the grid spacing in the three spatial directions. To avoid non-zero values of v_{sgs}at solid boundaries, a van Driest damping function [21] was used to specify ls as ls = $f_d C_s \Delta$, where f_d represents the damping function, varying along the normal direction of the wall.

Droplets

For the dispersed phase, the motion of water droplets was described by a Lagrangian approach. Due to the very low volume fraction occupied by the droplets, which never exceeds 0.1% and is often much lower, the droplets are assumed to have a unidirectional coupling to the speed range [40]. Thus, the flow influences their dynamics, but not vice versa. The position and velocity of each droplet were calculated from a set of differential equations, in which the droplets were considered rigid spheres, neglecting the transfer of heat and mass. Since each droplet was a simple point mass, its dynamics are expressed as:

$$\frac{dx_p}{dt} = u_p, \tag{7}$$

$$m_p \frac{du_p}{dt} = \sum F_i \tag{8}$$

where x_p is the position vector of the droplet, u_p is its velocity, and m_p is its mass. The term Σfi expresses the sum of all relevant forces acting on the droplet, and includes the dependence

on the velocity of the fluid. In the present study, only 3 forces were considered: F_D, the dragging force exerted on the droplet by the continuous phase; F_B, the buoyancy force; and F_G, the gravitational force. Due to the small density ratio of air droplets of 10^{-3} and the low speed of acceleration of the flow, these three forces alone affect the dynamics of the droplets, while others can be safely overlooked [40]. The total drag force suffered by a droplet is expressed as follows:

$$F_D = \frac{3}{4}\frac{\rho}{\rho_P}\frac{m_p}{d_p}\,C_d\,(u-u_p)|u-u_p| \qquad (9)$$

where d_p is the diameter of the droplet and ρ_p is its density. The drag coefficient C_d depends on the flow regime, and is a nonlinear function of the Reynolds number $Re_p = \rho d_p\,(u_p - u)$ based on the diameter of the droplet and the relative velocity. Here we use the following empirical relationship valid for spherical particles [40]:

$$C_d = \frac{24}{Re_p}\left(1+\frac{1}{6}\,Re_p^{2/3}\right); Re_p \leq 1000 \qquad (10)$$

Since for the cases considered in our study, it varies between 10^{-2} and 1, the previous expression does not significantly detach itself from the law of laminar motion $Re_p C_d = 24/Re_p$. Finally, buoyancy and gravitational force are defined together as:

$$F_B + F_G = \frac{(\rho_P - \rho)\pi d_p^3}{6}\, g \qquad (11)$$

Where g is the gravitational acceleration.

The computational setup

All numerical simulations were performed on the Galileo system (2 Intel Haswell processors at 8 cores per node, running at 2.40 Ghz) of the CINECA super-computing center, using 32 to 96 processors.

The first CFD analysis focused on the distribution of air flow and the deposition of droplets inside the nasal cavities during breathing (both during inspiration and expiration). The 3D meshes were built with 3 million cells, and nasal flow was simulated for 0.6 sec for both inhalation and expiration. Although constant limit conditions have been imposed, with a flow rate of 450 ml/s, the air flow simulated was unstable. Statistical averages and time fluctuations around the average are examined as follows.

Five coronal sections were analyzed for each patient (corresponding to the head of the lower turbinate, choana, and three sections equidistant to these two extremes). The nasal cavities were then equally divided into 3 axial regions (upper, middle and lower). For each coronal section and axial region, it was calculated: 1) the value integrated into the space of the flow fraction passing through the region and 2) the value integrated into the space of the turbulent kinetic energy k, e.g. a quantitative indication of the intensity of temporal fluctuations within the flow.

The second CFD analysis focused on the analysis of particle deposition at the level of the nasal mucosa, with particular attention to the olfactory groove (fig. 4).

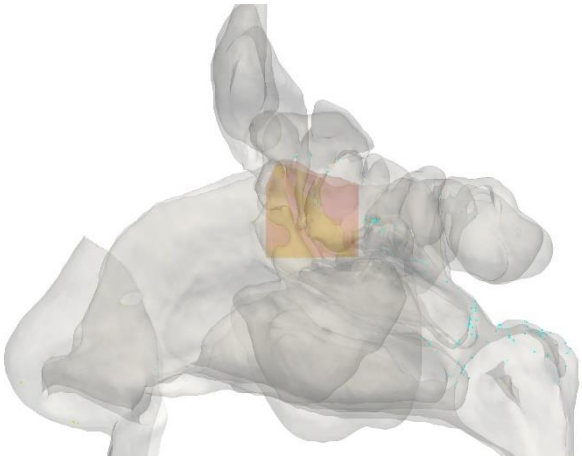

Figure 4 Volumetric reconstruction of the nasal cavities, with the area corresponding to the olfactory dimple highlighted

This analysis was not intended to define quantitative values, i.e. for example the absolute number of particles deposited in a certain segment of the mucosa, but a probabilistic datum, i.e. the probability that particles and consequently the virus will settle at the level of a certain portion of the nasal mucosa. Simulations were performed with a larger mesh, 25 million cells, significantly increasing accuracy. In this case lower flow rate of 220 ml/s was imposed, which is however still considered typical of medium intensity breathing [41]. For these simulations, droplets with a diameter of 1 µm and 5 µm were used, in accordance with the expected size of the droplets, as above mentioned [42]. Due to their inertia, droplets transported by the air flow might land on the mucosal membrane. The simulations recorded the number of droplets deposited, and then provided a vivid representation of the deposition pattern, highlighting the preferential deposition areas.

Results

The spatial distribution of the air flow (fig. 5) is markedly asymmetrical in the entire nasal fossa.

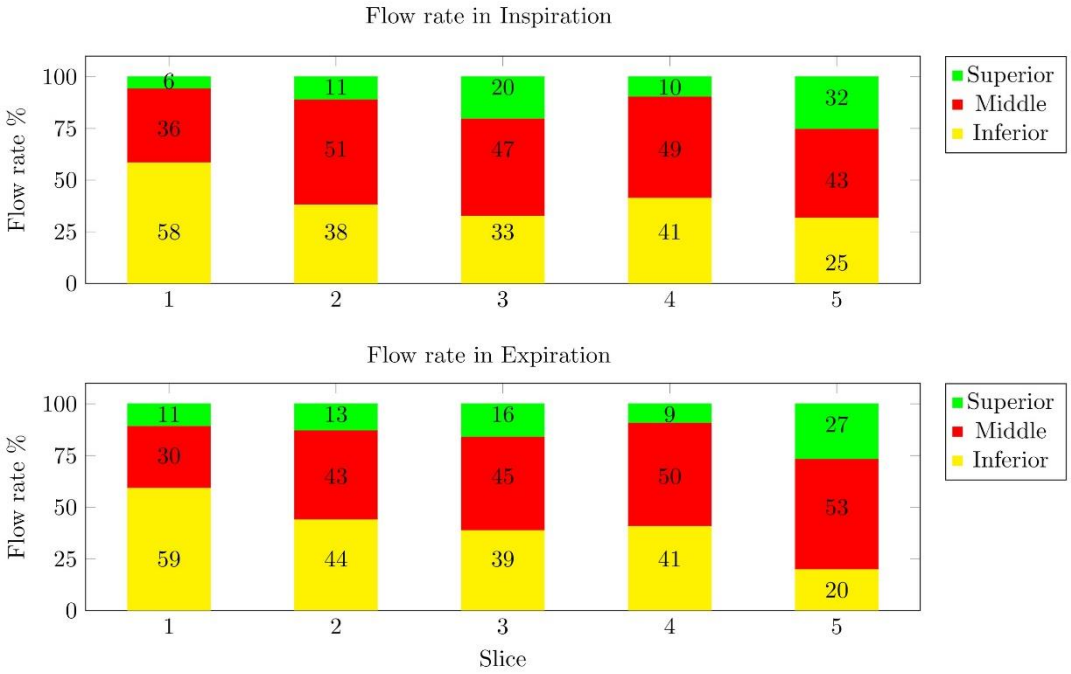

Figure 5 Mean percentage distribution of the air flow through the three horizontal partitions, in the five coronal sections considered. The upper graph refers to the inhalation, the lower to the expiration.

In particular, close to the nostrils and the inferior turbinate head, the inspiratory flow is distributed 58% in the lower horizontal partition, 36% in the middle and only 6% in the upper one, while in expiration the percentages are respectively 59% - 30% - 11%. At the level of the coronal sections 2, 3 and 4, corresponding to the central portions of the nasal cavities, the situation changes as the flow is distributed more to the middle horizontal partition than in the lower one, especially during inhalation. More precisely, the percentage of flow at the level in the middle partition is 51%, 47% and 49% during inhalation, respectively in sections 2, 3 and 4, while it is 43%, 45% and 50% during expiration. The percentage of flow distribution at the level of the upper horizontal partition remains even in these sections, both in inhalation and in

expiration, but with a progressive percentage increase up to the third coronal section (corresponding to the olfactory mucosa), in which it settles on 20% in inhalation and on 16% in expiration. At the level of the fourth section, the distribution percentages are almost comparable to the second section.

In the fifth coronal section, corresponding to the choanal region, air flow markedly increased in the upper horizontal segment both in inhalation (25% - 43% - 32% in inspiration and 20%-53%-27% in expiration).

Data on the turbulent kinetic energy k, graphically represented in Figure 6, provides interesting information about the nasal flow, and its being laminar or turbulent in various regions of the nasal cavities. Particularly, k is generally rather low in the first nasal portions, although slightly higher in the section 1 during inhalation and in section 4 during expiration, while it is strongly increased in section 5, during expiration. k reaches the lower values in section 3, of maximum interest for the current study, both in the inspiratory and expiratory phases. Moreover, k is very low in the upper horizontal region (olfactory groove).

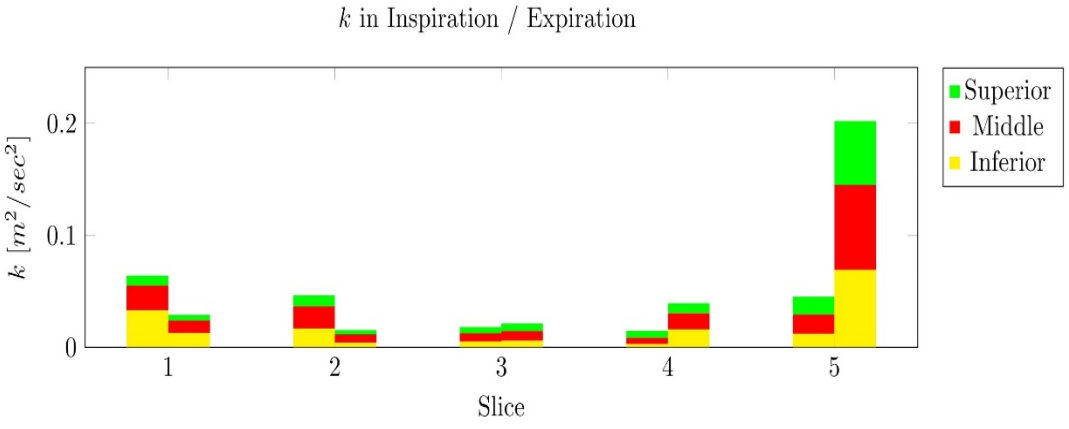

Figure 6 Mean distribution of turbulent kinetic energy k across the three horizontal regions, in the five coronal sections considered. The Left Column represents the inhalation, the right column the expiration.

The simulations performed on the second group patients are represented in figure 7, 8 and 9, respectively, shown in sagittal, axial and coronal projection, with comparison with the corresponding original CT scans. Blue droplets represent inhalation, while red droplets represent expiration. Analyzing the first figure (fig. 7), it is observed that the area where hypothetically the droplet / virus would be most likely to settle corresponds to the nasal vestibule and the head of the middle turbinate during inhalation, while in expiration the probability is maximum on the nasopharynx, the tail of the middle and the upper turbinate. On the olfactory mucosa droplets are few, but not absent, and especially present during the expiratory phase. Note that only for this series of projections it was chosen to show the left nasal fossa, to avoid the effect of overlapping in transparency of the two pits, otherwise inevitable. Three-dimensional models were always analyzed bilaterally. The analysis of axial projections (fig. 8) confirms the higher concentration of particles in the anterior segments during inhalation and in the posterior ones during expiration. On this projection, it is confirmed that the droplets have a higher probability of impacting and adhering to the mucous membrane of the olfactory groove during expiration, rather than inhalation. Finally, the analysis of coronal projections (fig. 9) confirm the data observed so far, but allowing a better visualization of the region of the septal rostrum and of both portions of the nasopharynx. In this projection, the presence of a few particles at the level of the olfactory groove is confirmed, almost exclusively during expiration.

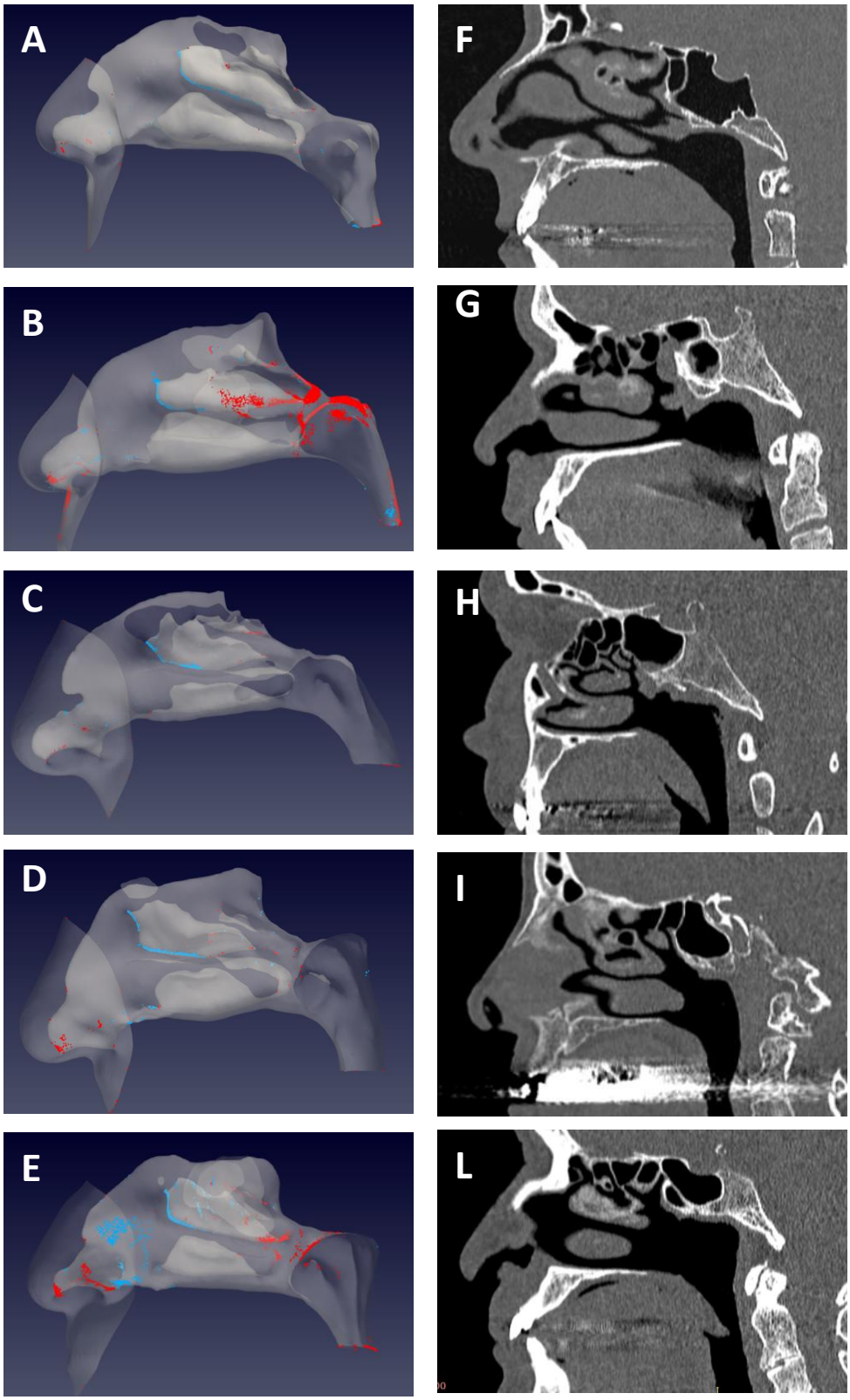

Figure 7 Probabilistic distribution of droplets from 5µ in inhalation (blue) and expiration (red), sagittal projection. The A-E subunits show 3D models of the left nasal fossa alone, obtained from the original CT scans of five patients, reported in the F-L subunits. Each 3D model is related to the corresponding TC image. The droplets size has been increased to improve clarity.

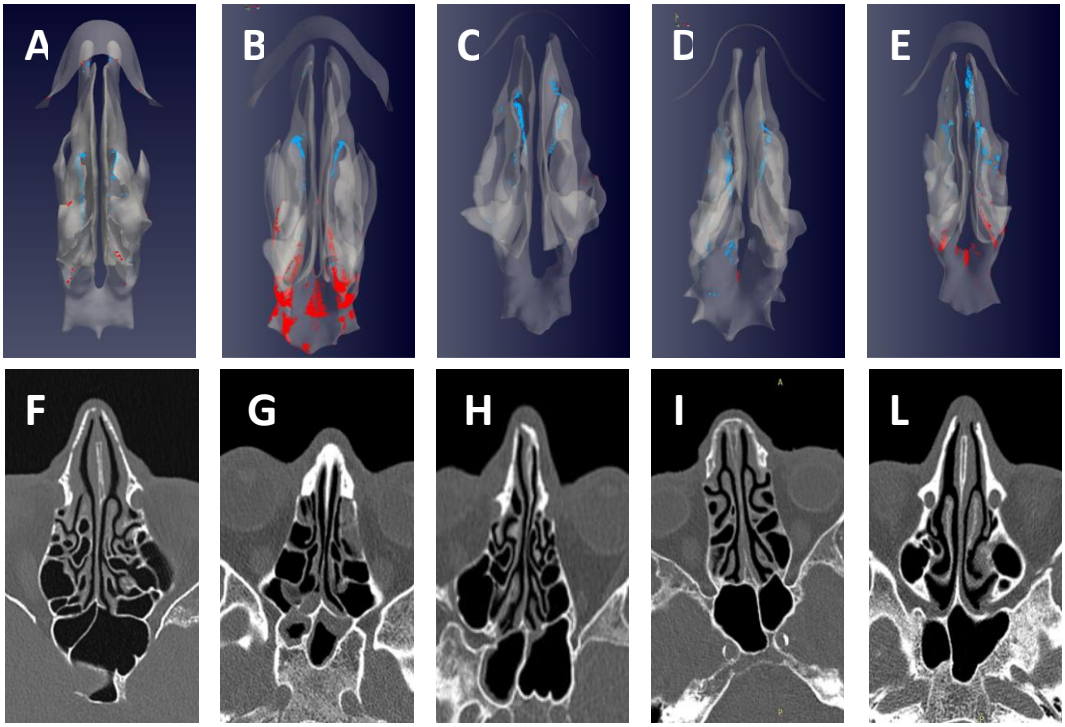

Figure 8 Probabilistic distribution of droplets from 5µ in inhalation (blue) and expiration (red), axial projection. The A-E subunits show 3D models of both nasal cavities, obtained from the original CT scans of five patients, reported in the F-L subunits. Each 3D model is related to the corresponding underlying CT image. The droplets size has been increased to improve clarity.

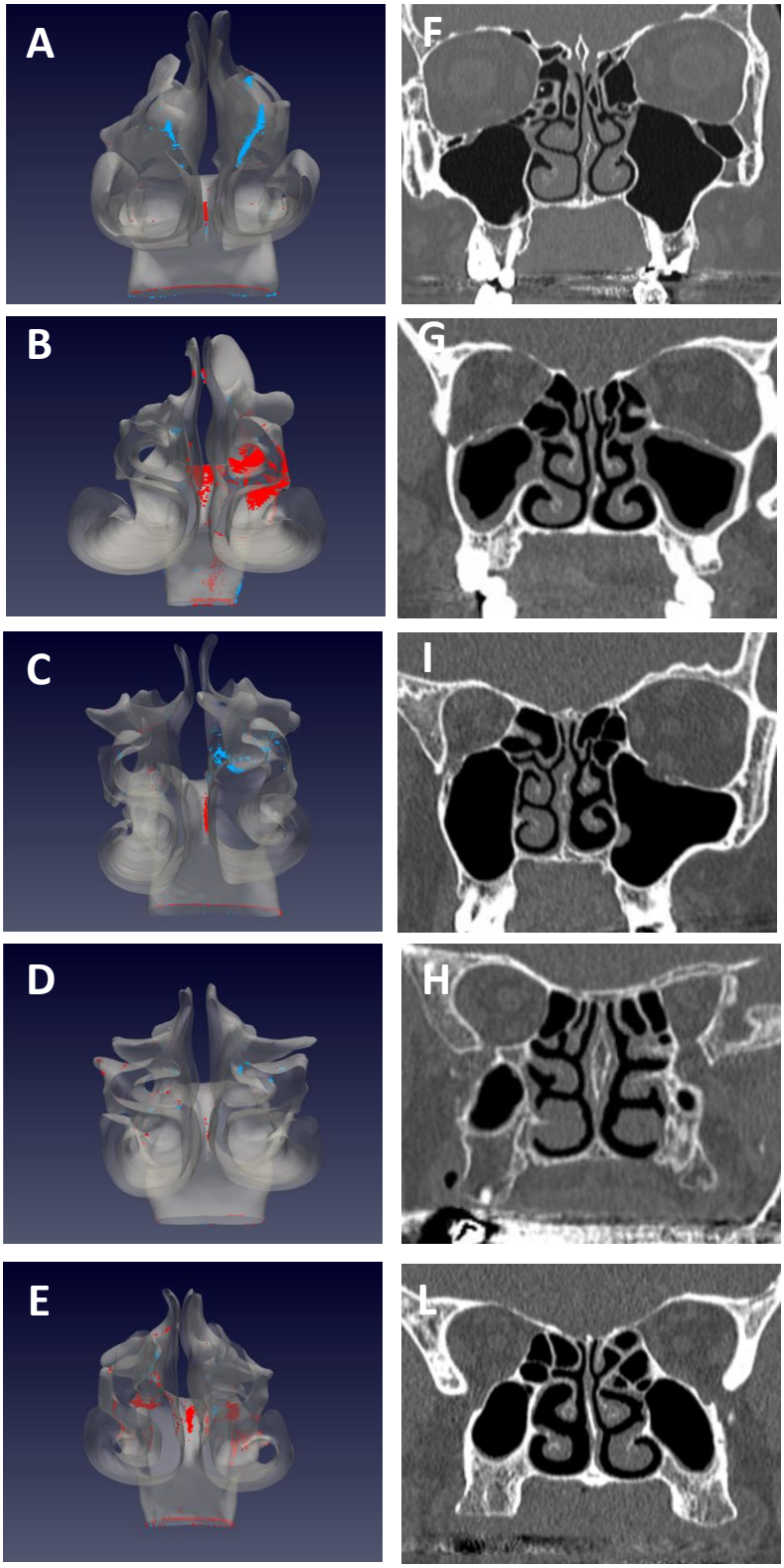

Figure 9 Probabilistic distribution of droplets from 5μ in inhalation (blue) and expiration (red), coronal projection. The A-E subunits show 3D models of both nasal cavities, obtained from the original CT scans of four patients, reported in the F-L subunits. Each 3D model is related to the corresponding TC image. The droplets size has been increased to improve clarity.

Discussion

Regardless of the mode of viral transmission (direct respiratory, aerosol, or fomite), initial access to the nose must be made during inhalation. Once the virus has gained access to the sinonasal cavity, it can spread via a variety of routes, including transport, local replication, and invasion of nearby structures. SARS-CoV-2 has been demonstrated to bind the ACE-2 receptor, enter respiratory epithelial cells, and therefore initiate replication[43,44]. The olfactory cleft should not be considered a primary target for COVID-19 infection because virus-carrying respiratory droplets cannot reach there in significant numbers. The olfactory cleft is biologically designed to absorb smaller particles, such as odorants, while droplets carrying the viral load may be larger [45]. Such an ineffective viral deposition onto the olfactory mucosa, in conjunction with the known defensive mechanisms employed by the olfactory mucosa to protect against environmental noxae [43,46], renders the direct infection of the olfactory cleft by SARS-CoV-2 at the time of primary entry into the organism improbable at best. In contrast, cumulative exposure of the olfactory cleft to expiratory droplets from the lower respiratory tract may be more probable in organisms that have previously been ill. The viral load in the lung is significantly greater than that of an aerosol entering the nose. The act of expiration occurs tens of thousands of times per day, and the source of contamination acts continuously for several days. This pathway to the olfactory cleft and possibly the central nervous system may also explain the delay between the onset of the initial symptoms and the onset of the first neurological abnormalities, such as hyposmia [47,48]. Infection of the central nervous system by SARS-CoV-2 through the olfactory mucosa may be the result of a disease of the lower respiratory tract, as suggested by the current findings. Infected individuals should therefore consider preventing virus penetration of the olfactory mucosa. High volume nasal washes, typically performed with saline, can be used to minimize the adhesion of viral components

released from the lower respiratory tract to the nasal cavity, thereby diminishing the virus's ability to spread to the olfactory mucosa. Some authors have recommended nasal lavages as a preventative measure against SARS-CoV-2 infection. Infection of the central nervous system by SARS-CoV-2 through the olfactory mucosa may be the result of a disease of the lower respiratory tract, as suggested by the current findings. Infected individuals should therefore consider preventing virus penetration of the olfactory mucosa. High volume nasal washes, typically performed with saline, can be used to minimize the adhesion of viral components released from the lower respiratory tract to the nasal cavity, thereby diminishing the virus's ability to spread to the olfactory mucosa. Some authors have recommended nasal lavages as a preventative measure against SARS-CoV-2 infection. Infection of the central nervous system by SARS-CoV-2 through the olfactory mucosa may be the result of a disease of the lower respiratory tract, as suggested by the current findings. Infected individuals should therefore consider preventing virus penetration of the olfactory mucosa. High volume nasal washes, typically performed with saline, can be used to minimize the adhesion of viral components released from the lower respiratory tract to the nasal cavity, thereby diminishing the virus's ability to spread to the olfactory mucosa. In fact, some authors have recommended nasal lavages as a preventative measure against SARS-CoV-2 infection [49], and previous research on viral upper respiratory tract infections with hypertonic saline has demonstrated a reduction in viral shedding and patient infectiousness [50] in the diseased. Others propose other types of medications [51]: It is suggested that acetic acid be inhaled to shorten the duration of symptoms. In addition to suggesting the olfactory region as a target for inhibition of the secondary viral infection that threatens the CNS, the present study provides additional evidence for the effectiveness of such preventive measures, as a diffuse droplet deposition occurs in the nasal fossae, which can be easily reached by washing or other nasal medications.

Conclusion

Using CFD, a distinct droplet distribution and a novel spectrum of information on the distribution of physiological nasal flow have been established. CFD, in contrast to all previous methods, has made it possible to evaluate various nasal regions and portions, delivering accurate and timely data. This new tool can provide answers to a variety of questions and has a wide range of applications.

5. Computational Fluid Dynamics in Turbinate surgery

Introduction

Until a few years ago, a key concept in turbinate surgery was: “More intranasal space equals improved nasal breathing”. Nowadays, the increased knowledge of the consequences of invasive surgery is leading surgeons towards more conservative approaches [52.] Total Turbinectomy is still considered a viable approach in a few cases, such as endoscopic medial maxillectomy (EMM) [53]. The main functional complications of aggressive surgery are crusting and the Empty Nose Syndrome (ENS), which is a complex medical condition characterized by the perception of nasal obstruction despite non-restricted post-surgical nasal spaces [12,54,55]. ENS is not a trivial condition, and it leads to important morbidity, as it deteriorates the quality of life, causes anxiety, depression, and even nasal aprosexia [13]. Several therapeutic approaches have been proposed, with conflicting results [56,57]. The etiology of ENS remains elusive. Some authors believe that ENS is due to alteration of the trigeminal sensory functions [58,59], others identify the altered perception of the mucosal wall shear stress (WSS) as leading cause [60,61]. A local increase of WSS may also be responsible for crusting, due to the shear-induced damage to the mucosa. Some authors postulate the loss of temperature perception as an important etiological factor [60]. The analysis of airflow characteristics has been challenging since the last years, but nowadays, CFD can solve this issue.

This chapter focuses on velocity and vorticity fields in the nasal fossae and discusses the potential pathogenic significance of turbulent vortical structures in the ENS. The particular objective is to establish if the study of DNS-computed flow fields may be used to evaluate the fluid dynamics of the sinonasal cavity following partial and entire inferior turbinate (IT) resections. The outcomes of DNS and RANS simulations will be contrasted and discussed

critically. In addition, we explain the concept and provide an example of virtual surgery. The computer models will be changed to simulate various surgical procedures, and the corresponding air flow adjustments will be shown.

Methods

Geometrical models

The CT scan of a 67-year-old male presenting a normal sinonasal anatomy was selected. The scan contained 348 DICOM images, with spatial resolution of 0.5 mm × 0.5 mm in the sagittal–coronal directions, and a 0.6 mm axial gap between consecutive slices. CT images were converted into an accurate geometrical, as widely discussed in the previous chapter. The original anatomy reconstruction was used as baseline pre-op reference (figure 10)

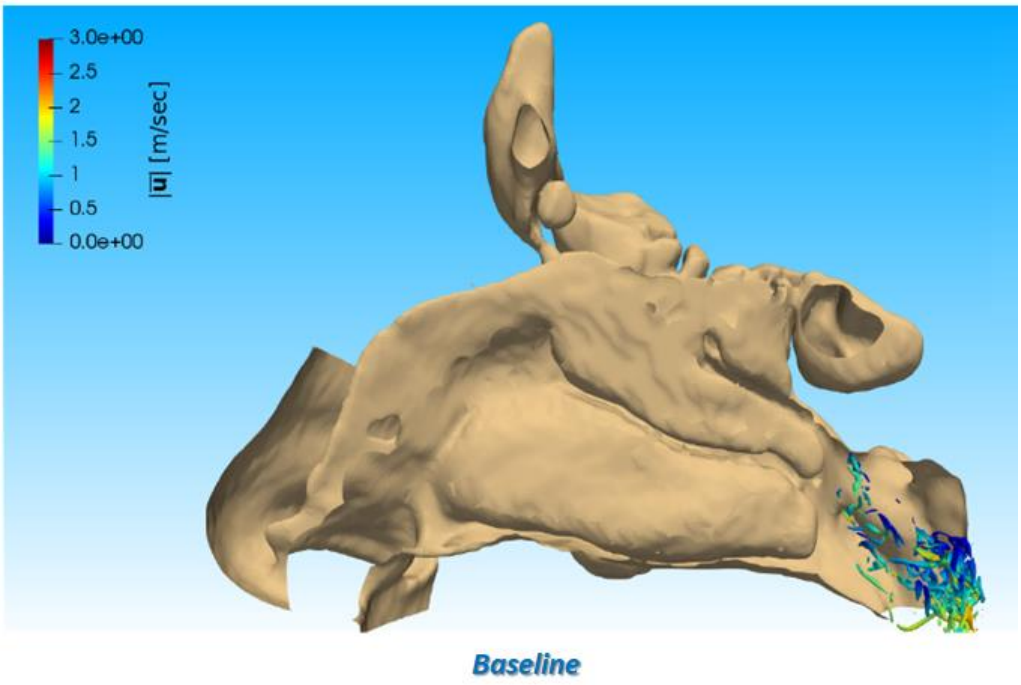

Figure 10. Instantaneous flow field in the baseline right nasal fossa anatomical model. The colors of the iso-surfaces visualize turbulent vortical structures, which are mainly concentrated in the posterior area. The color of the structures indicates the magnitude of the velocity vector, shown by the color-bar (top left).

Using the 3DSlicer® software [34–36], the baseline 3D model was further modified to obtain six models where virtual surgery was enforced to various degrees on the patient's right side. The septum and the left side of the nasal cavity remained untouched. In the three turbinoplasty

cases, we progressively removed more tissue from the IT (case 1: 0.5 cm from the head of the IT; case 2: 1.5 cm, case 3: 3 cm). In the total right turbinectomy model (case 4), the whole IT was removed, entirely exposing the lateral wall of the inferior meatus. In case 5, the middle right turbinate and the meatus were completely removed. Case 6 represents a particular turbinoplasty, where the main part of the IT was removed, but the turbinate head was preserved (Table 1)

CASE	VIRTUAL SURGERY INTERVENTION	ANATOMICAL CHANGES AFTER SURGERY
0 (BASELINE)	None	None
1	Inferior turbinoplasty 1	Removed 0.5 cm from the head of inferior turbinate (IT)
2	Inferior turbinoplasty 2	Removed 1.5 cm from the head of IT
3	Inferior turbinoplasty 3	Removed 3 cm from the head of IT
4	Total inferior turbinectomy	Whole IT removed
5	Total middle turbinectomy	Whole middle turbinate removed
6	Inferior turbinectomy with head preservation	Body and tail of IT completely removed, with preservation of the head.

Table 1 models considered in the study, together with the type of virtual surgery over the baseline model and the consequent anatomical changes.

Simulations

The airflow in the reconstructed nasal cavities was simulated with the open-source CFD software OpenFOAM® [38]. The computational volume was discretized by 50 million cells. To visualize turbulent vortical structures, the commonly accepted lambda2 method was employed [61,62]. This method was used to highlight vortical features within the flow [63], and it has been widely used in literature to describe human nasal airflow [64–66]. A companion RANS analysis was also carried out for the same anatomies, but on a smaller computational mesh (9 million elements). The turbulence model was the often-employed k-omega-SST [67].

To assess the post-operative outcome, all seven cases were simulated under identical conditions: a steady inspiration lasting 0.6sec, driven by a pressure difference of 20 Pa between the external ambient and the laryngeal area. The simulation employed no-slip and no-penetration boundary conditions at the wall, and a zero-gradient velocity boundary condition at the outlet. Although the boundary conditions were steady, the DNS solution is time-dependent and captures the temporal dynamics of the flow. However, the mean and other statistics of the flow can be computed *a posteriori* by a process of time-averaging, which is analogous to real experimental measurements. The main turbulent vortical structures were colored according to the local magnitude of the velocity vector, so that their convection speed could be appreciated. Identical conditions are used for the accompanying steady RANS simulations, which however, by definition, only provide the mean fields.

Results

DNS simulation are shown in fig. 11

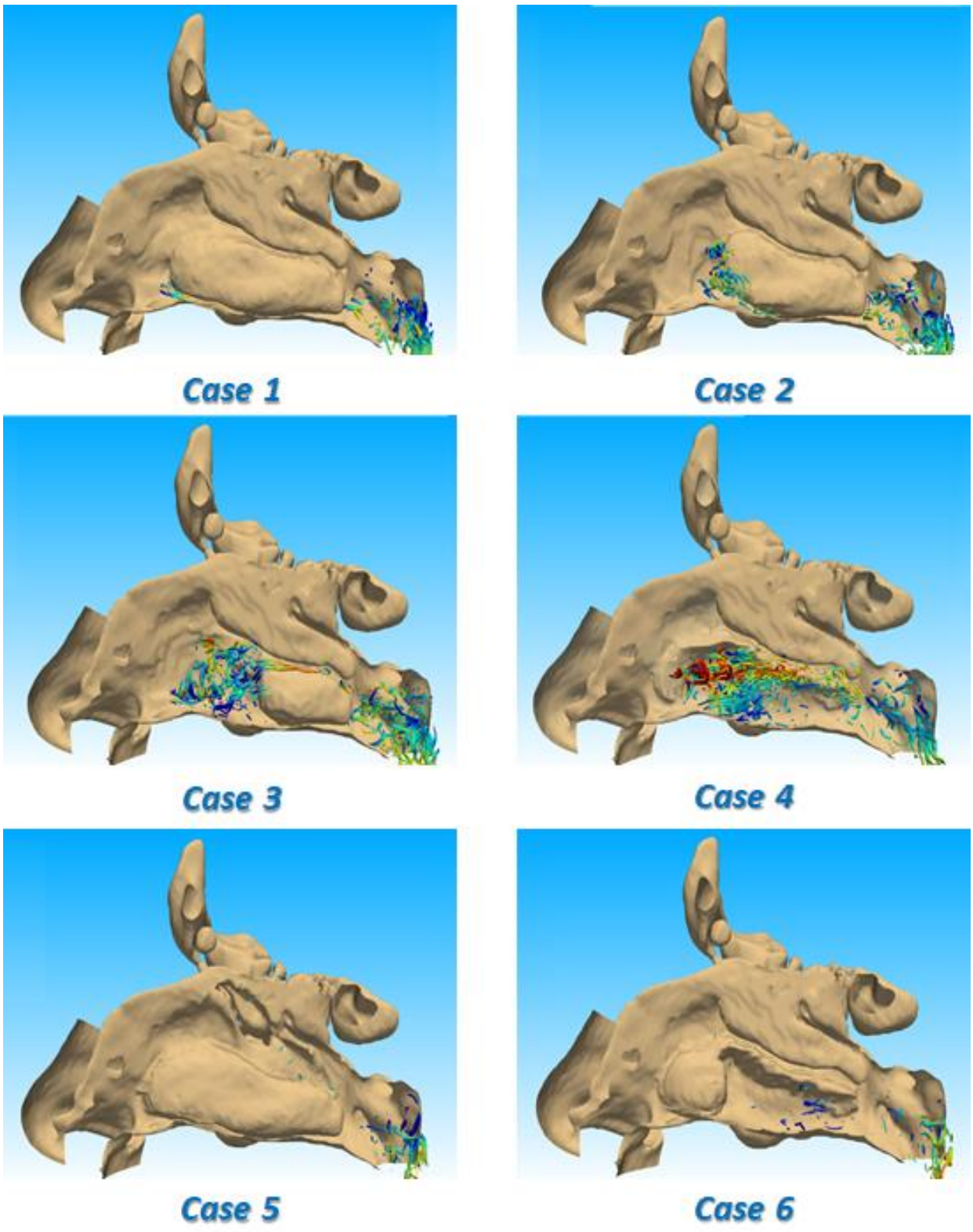

Figure 11 The six anatomical models derived from the baseline via virtual surgery: after turbinoplasty of various degrees (case 1,2,3), inferior turbinectomy (case 4), middle turbinectomy (case 5) and turbinoplasty with head preservation (case 6). Flow structures and colours as in Figure

In the baseline model, areas of turbulence are mainly in the rhinopharynx, posteriorly to the tail of the IT. The maximum velocity is less than 1.5 m/s. In case 1, a slight increase in maximum velocity of the vortical structures (up to 2 m/s) is registered, posterior to the tail of the turbinate. Tiny structures appear before the IT. In case 2, the vortices increase in number and convect faster (up to 2-2.5 m/s both anteriorly and posteriorly). They are found in a wider area of the upper part of the rhinopharynx, where they were absent before. In case 3, the vortices increase again in number and speed, both in front (up to 2.5 m/s in selected regions) and above the rear of the turbinate tail, where mainly the inferior stream increases in maximum velocity (almost up to 2 m/s). A turbulent vortical stream running above the turbinate and on the floor of the middle meatus can be observed, with an increasing anteroposterior velocity gradient (from 1.5 m/s to almost 2.5 m/s). In case 4, an important increase in turbulent activity is visualized along the whole lateral wall of the inferior meatus. The convection speed of the structures strongly increases, reaching a peak of 3 m/s in the anterior parts. In case 5, the middle turbinectomy does not affect the nasal flow, with only a reduced concentration of vortices in the anterior portion of the rhinopharynx compared to the posterior portion. In case 6, vortical structures are almost identical to the baseline, and only a few vortices can be identified in the opened inferior meatus. Vortical activity inside rhinopharynx is lower than in the baseline model. The RANS simulations, whose results are plotted in Figure 12, do not provide instantaneous data.

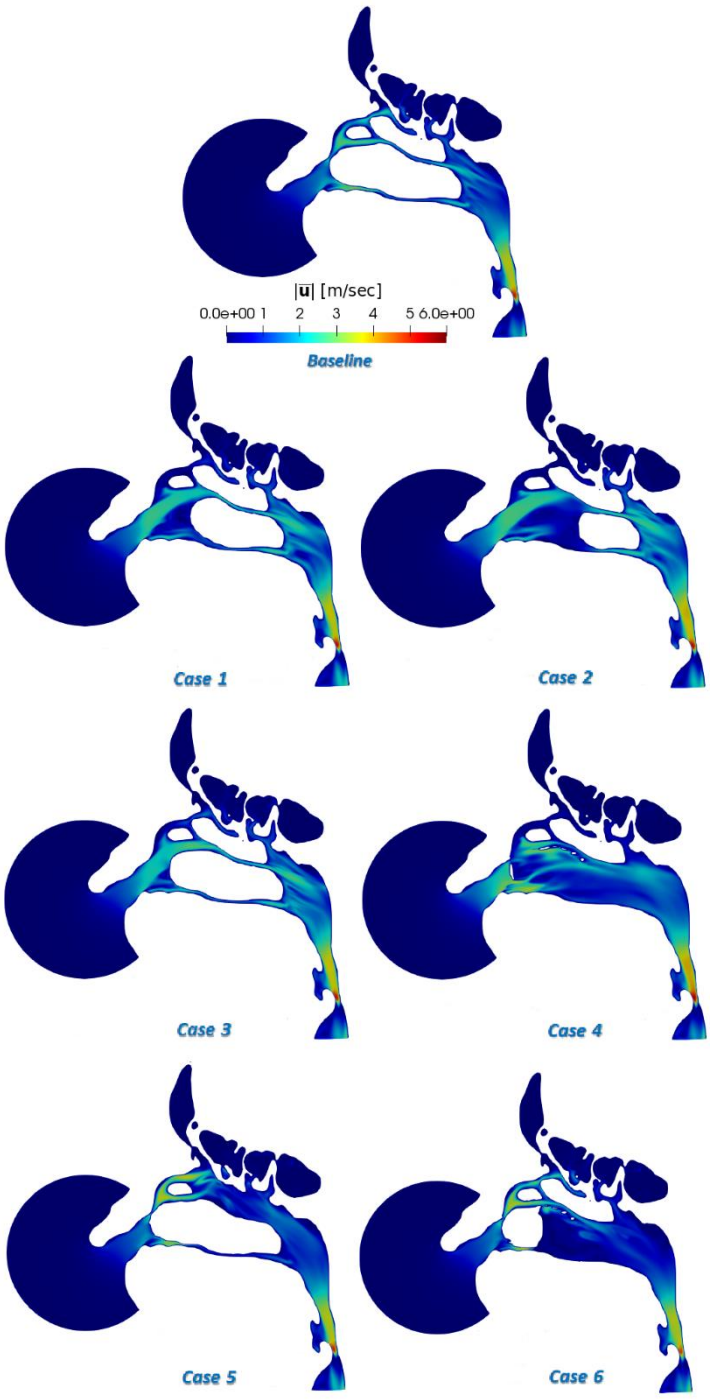

Figure 12 The mean velocity field in a sagittal section, for the baseline (top) and the operated cases.

Comparison between RANS and DNS has been performed on the results of flow rate (Q) calculation in all virtual models. The numerical results are listed in table 2.

	BASELINE	**1**	**2**	**3**	**4**	**5**	**6**
Q (DNS) [L/MIN]	7.168	8.514	9.021	10.024	10.898	7.357	7.106
Q (DNS) [> %]		(+18.8%)	(+25.8%)	(+39.8%)	(+52.0%)	(+2.6%)	(-0.9%)
Q (RANS) [L/MIN]	5.984	7.355	8.004	9.368	10.947	6.458	6.438
Q (RANS) [> %]		(+22.9%)	(+33.7%)	(+56.5%)	(+82.9%)	(+7.9%)	(+7.6%)
Δ DNS-RANS	-16.5%	-13.6%	-11.3%	-6.5%	+0.5%	-12.2%	-9.4%

Table 2: Flow rate in liters/minute passing through the operated right passageway, as computed from DNS and RANS. Percentage changes with respect to the baseline and percentage difference Δ between DNS and RANS results are also shown.

In models 1-5, both DNS and RANS showed increased Q compared to baseline, justified by progressive nasal space augmentation. It must be underlined that the numerical results showed consistent differences (table 2, bottom line). In case 6, we can observe not only an important numerical difference between the flow rates calculated with RANS and DNS (Δ -9.4%), but also a changeover from positive to negative of the percentage modification of case 6 compared to baseline (RANS: +7.6%, DNS: -0.9%).

Discussion

The objective of the present study is to analyze the modifications of the nasal flow field after different types of virtual turbinate surgery, by focusing on turbulent structures and their clinical implications. In the baseline situation, the airflow is laminar (albeit three-dimensional and unsteady) almost everywhere, becoming turbulent only in the rhinopharynx. Modification of the turbinates [68–70] , even minimal, is one of the major causes that alter the natural laminarity of the airflow. From our clinical experience, minimal alterations do not correlate to any particular complication or symptom, while more aggressive surgical approaches do. Mucosal and homeostatic alterations are significant in total turbinectomy, and may finally lead to ENS [12,71]. Patients usually experience reduced sensation of nasal flow. The nasal mucosa appears hyperemic and requires regular and long-lasting toilette to avoid infections or other complications [57]. IT prosthetics and inoculation of autologous or heterologous material under the mucosa of the nasal lateral wall are the main interventions proposed to treat ENS, in an attempt to recreate a normal bulging and restore a physiologic pattern of nasal airflow [57,72,73]. These procedures showed variable outcomes [11,57,72,73]. However, the link between flow regularization induced by the reduction of nasal spaces and the beneficial effect on ENS indicates the importance of turbulence as a cause of ENS, beyond impaired proprioception of the nasal flow.

Total middle turbinectomy can be proposed in case of turbinate degeneration (e.g. in the context of nasal polyposis) or excessive instability (e.g. during extensive endoscopic sinus surgery). This procedure is not associated with relevant morbidity or complications [72,74] and is usually - but not ubiquitously - accepted. Our analysis of the resultant nasal flow shows little difference in the baseline, with a generally near-normal flow quality. Thus, total middle

turbinectomy, as advocated by the European position paper on rhinosinusitis [17], can be considered to have a non-significant impact on nasal physiology.

Case 6 represents a peculiar condition, where an aggressive surgery on the IT, almost totally removed except for its head, is associated with limited flow changes. From our clinical experience, such an approach guarantees a low complication rate, with only a few cases of nasal dryness, and no significant rise in ENS or diffuse nasal crusting. We suggest that the preservation of the turbinate head leads to a normal velocity field around the nasal fossa, such that the flow remains laminar almost everywhere, and consequently the WSS fluctuations are reduced. Comparing cases 4 and 6 to the baseline model, the different nasal flow alterations are evident, although the volume of the removed turbinates is almost the same, perhaps explaining the higher complication rate in clinical practice.

Another point of the present paper, which faces an important methodological matter in nasal CFD, is the comparison with RANS results. Figure 12 is a classic visualization of RANS, which results in a sagittal section. A comparison with figures 11 and 12 emphasizes the limited information content of RANS results, where the various cases can be barely discerned in terms of the mean flow field. In particular, the time-averaged flow field provided by RANS is unable to describe instantaneous vortical structures, which are easily appreciated with the DNS model, and account for the most important variations induced by turbinate surgery. Moreover, RANS contains a potentially significant modeling error. Table 2 and Figure 13 in easier, graphical form show the difference of a simple, global quantity as the flow rate through the operated side.

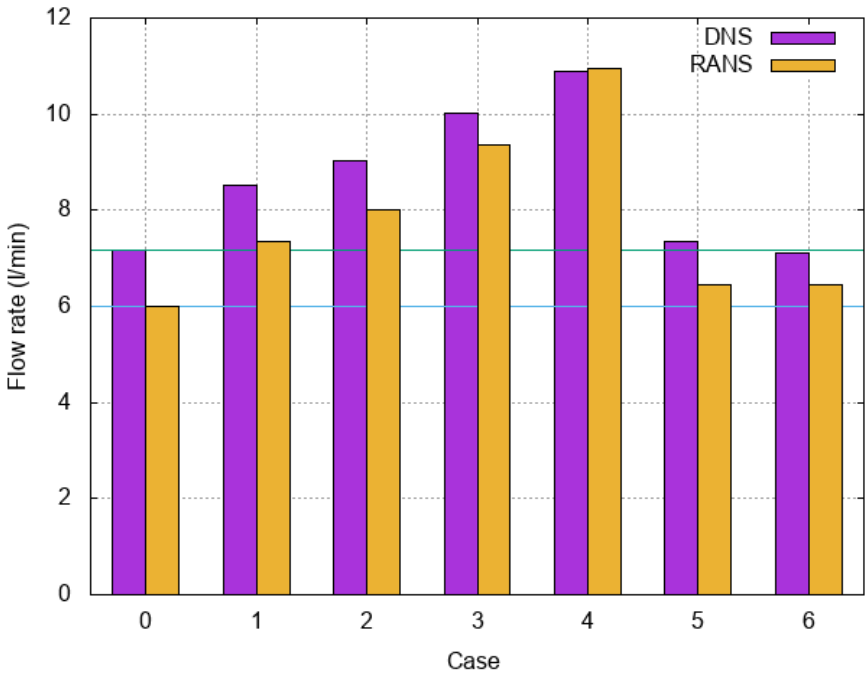

Figure 13 . Graphical representation of data reported in Table 2: for the baseline and the 6 modified anatomies, values of the flow rate in the operated passageway, computed with DNS and RANS.

Obviously, there is always an increment in baseline, since surgery leads to an increase in the cross-sectional area. Case 5 and 6 are confirmed to be the less invasive ones. The key observation, however, concerns the considerable quantitative difference between RANS and DNS results, leading to a 17% overestimate of the nasal resistance by RANS in the baseline case. Even more importantly, this overestimate is not a simple offset, as the modeling error implied by RANS changes when the flow physics changes. The extreme example is case 4, where differences between RANS and DNS change sign, with RANS predicting a slightly smaller nasal resistance than DNS. As a result, our study suggests DNS is a first-choice tool to study nasal fluid dynamics, especially in pathological alterations of the anatomy.

Our study has limitations. First, a single anatomy modified by virtual surgery was used; a large sample size is necessary to consolidate our findings. However, since the baseline sinonasal anatomy represents a normal anatomy, our results describe the effects of multiple surgical

modifications on a normal nose. Despite the study being carried out on a single anatomy that limited the statistical significance of the results, we believe that a major strength of our study is the use of a rigorous methodology and robust modeling that guarantee instant and reliable information. Furthermore, as already shown in previous works [75], the DNS computation offers unique information that lacks modeling mistakes, such as those related to time dependency.

Conclusion

This study discussed the changes of instantaneous nasal airflow after inferior and middle turbinate surgery, and their clinical relevance. The employed state-of-the-art numerical technique vastly improves above the conventional RANS approach and provides the opportunity to examine instantaneous flow fields with the associated vortical turbulent structures. IT surgery is often considered banal, but both clinical experience and the results of our study suggest some pitfalls exist. Our data shows how preservation of the head of the IT could be fundamental to preserve the flow quality, even when massive demolition of its posterior parts is performed. Conversely, the middle turbinate can be widely modified without significant complications.

CFD-based observations overlap clinical findings, demonstrating the importance of time-resolved CFD studies to investigate the complex problem of nasal ventilation posed by ENS surgery, which is mainly approached empirically nowadays. We believe that high-quality CFD tools will be increasingly important in ENT practice, thanks to their unique ability to non-invasively assess the functional, anatomical, aerodynamic characteristics of the nose in each patient using an individualized approach.

6. Partial Preservation of the Inferior Turbinate in Endoscopic Medial Maxillectomy

Introduction

Since its introduction [76], endoscopic medial maxillectomy (EMM) has become a staple procedure in the management of maxillary sinus (MS) neoplasms [77]. Furthered by technical refinements [78], EMM is also employed to address selected inflammatory conditions. EMM shows solid surgical results [79,80], but it has known minor issues (crusting, lacrimal pathway obstruction, and malar region hypoesthesia) [81]. To address them, several types of modified EMM (M-EMM) have been proposed [82–85], aimed at sparing the lacrimal pathway and the inferior turbinate (IT). IT preservation is commonly thought to preserve its role in temperature adjustment and nasal airflow control [86,87]. Conversely, whole turbinate resections lead to persistent crusting and reduction of inhaled air conditioning [82]. Anecdotal reports support such observations and subjective surgical outcomes analysis [82,88], but no study thoroughly addressed the role of IT resection and partial preservation in EMM from a fluid dynamical standpoint. Few literature studies provided numerical models of EMM built via computational fluid dynamics (CFD) [89]. In particular, Lindemann et al.[90] hint at the presence of large vortical structures in the MS after EMM. Their computational design limits such CFD studies, relying on rather simple mathematical models, unable to simulate the fluctuating quantities. While the IT role has been studied with different in vitro and computational models [91,92], suggesting chaotic and/or vortical flow patterns in the nasal cavity after aggressive turbinate resections, no studies mirrored these changes in EMM patients. This study was conducted with a DNS approach. A solid theoretical foundation for EMM modifications will thus be provided.

Methods

As mentioned above, the airflow in the reconstructed nasal cavities was simulated via the open-source CFD software 3D-Slicer® and OpenFOAM® [34–36,93]. The scan of a 67-year-old man presenting a normal sinonasal anatomy was selected. The CT scan contained 348 DICOM images, with spatial resolution of 0.5mm x 0.5mm in the sagittal-coronal directions, and a 0.6-mm axial gap between consecutive slices. CT images were converted into an accurate geometrical model via 3D-slicer® [34–36], choosing a proper radiodensity threshold [37]. A 3D computational domain was then built, according to the procedure illustrated in previous chapters. The anatomy reconstruction was used as the baseline pre-op reference and formed the basis for 2 additional virtual surgery anatomies (see Results for details), providing a model of standard EMM and M-EMM. Each of the 3 cases was then discretized onto a 50-million cell volume mesh, corresponding to an average spatial resolution of 200 µm. The 3 cases were simulated under the same conditions, using the DNS of the Navier-Stokes equations to assess the postoperative outcomes: a steady inspiration, lasting 0.6 seconds after statistical equilibrium, driven by a pressure difference of 20 Pa between the external ambient and the laryngeal region. The simulation employed no-slip and no-penetration boundary conditions at the wall and a zero-gradient velocity boundary condition at the outlet. With a time step size of $1x10^{-5}$, each simulation required $6x10^{4}$ steps to complete. Using the 3D-Slicer® software, the original 3D model was reprocessed to obtain 2 virtual surgery models (fig 14). The 2 models represent an EMM and an M-EMM performed on the patient's left side. In the EMM model, mimicking common approaches for sinonasal neoplasms, the whole IT, the MS medial wall, the uncinate process, and the middle turbinate were removed, sparing middle turbinate superior and lateral insertions; the ethmoid bulla was opened. In the M-EMM model, the anterior portion of the IT and the anterior portion of the medial MS wall up to the nasolacrimal

duct were spared, as proposed in various models [82]. All the other modifications were replicated from the EMM model.

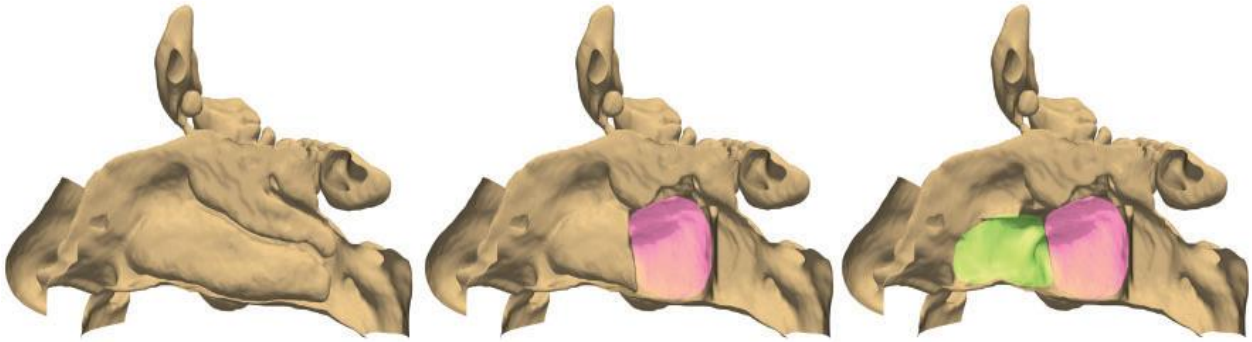

Figure 14 The 3 anatomies considered in the present study: the baseline model (left), the anatomy after virtual EMM (right), and the conservative virtual M-EMM (center) where the anterior part of inferior turbinate and maxillary sinus were spared. Colors indicate the affected anatomical regions: pink highlights the lateral nasal wall demolition of M-EMM, while green indicates the further demolition required for EMM. EMM, endoscopic medial maxillectomy; M-EMM, modified endoscopic medial maxillectomy

Results

The comparative CFD analysis of the 3 models reveals evident changes in the airflow patterns after EMM, while M-EMM presents general features more closely resembling the baseline.

Volumetric Flow Rate and Velocity

The first and foremost difference is how EMM induces a higher increase in the flow rate of the operated (left) side (see Table 3) than M-EMM model.

	BASELINE	**M-EMM**	**EMM**
Q RIGHT (L/MIN)	9.223	8.760 (-5.0%)	6.983 (-24.3%)
Q LEFT (L/MIN)	6.738	8.290 (+23.0%)	11.612 (+72.3%)
Q TOT (L/MIN)	15.961	17.048 (+6.8%)	18.595 (+16,5%)

Table 3 : Abbreviations: EMM, endoscopic medial maxillectomy; M-EMM, modified endoscopic medial maxillectomy. The table reports the quantitative flow rate of the non-operated (right) side, for the operated (left) side, and the overall quantitative flow rate for the assigned pressure drop. The flow rate increase in the operated side is less obvious in the M-EMM model.

Second, as shown in Figures 15 and 16, in the baseline model, the highest velocity region is located in the middle meatus.

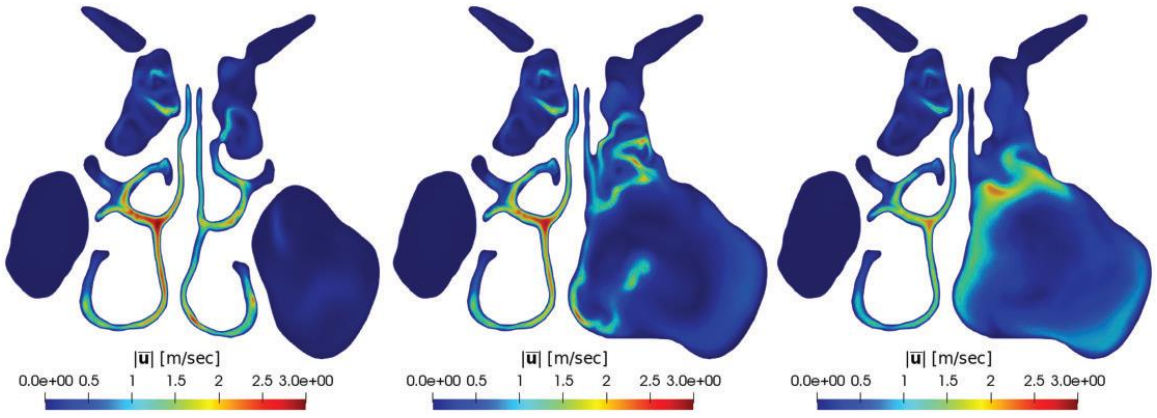

Figure 15 Magnitude of the mean velocity field in a coronal plane passing through the volume interested by surgery. From left to right: baseline, M-EMM, and EMM.

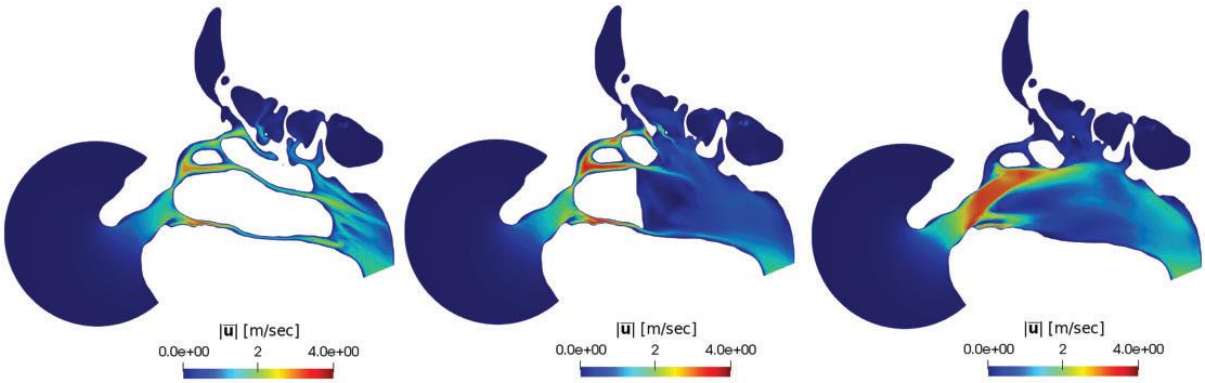

Figure 16. Magnitude of the mean velocity field in a sagittal plane. From left to right: baseline, M-EMM, and EMM.

EMM induces a substantial alteration of the mean velocity field in the operated side, showing higher velocity in the MS lateral and cranial portion. Furthermore, EMM reduces the maximum velocity and flow rate in the contralateral side. Conversely, in M-EMM, the mean velocity field does not present increased velocity areas, and the contralateral side remains essentially unchanged. Last, the larger the turbinate resection, the more streamlines penetrate the MS, as shown in Figure 17.

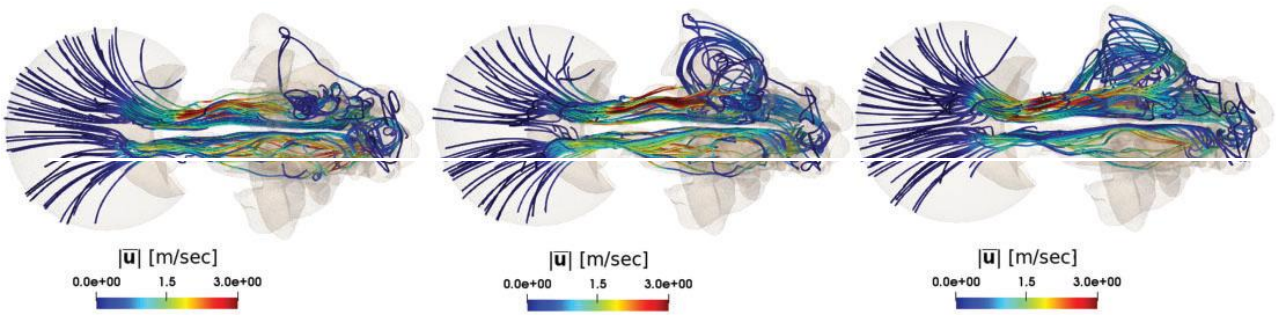

Figure 17. Three-dimensional view of the streamlines in the baseline (left), M-EMM (center), and EMM (right) cases. Streamlines departing from the outer ambient are observed to progressively enter the right maxillary sinus as the turbinate resection becomes more substantial. Streamlines are colored with the local magnitude of the velocity vector.

Fluctuations

Our time-resolved simulation provides information on flow unsteadiness, quantified here by the root-mean square (RMS) values of the fluctuations of the velocity magnitude. As shown in Figures 18 and 19, in the baseline model, the RMS value in the inferior and middle meatus is negligible, suggesting a nearly steady flow.

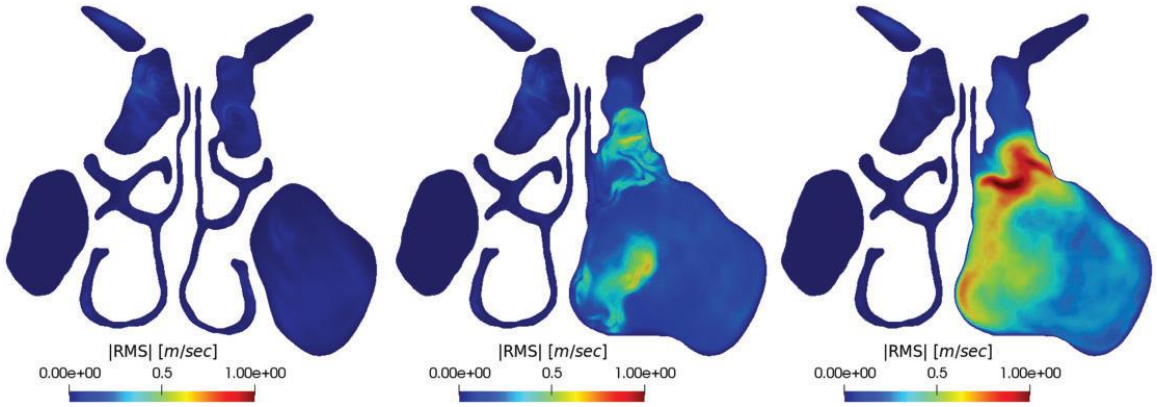

Figure 18 2 Root-mean-square value of the fluctuations of the velocity magnitude in a coronal plane. From left to right: baseline, M-EMM, and EMM. RMS, root-mean-square

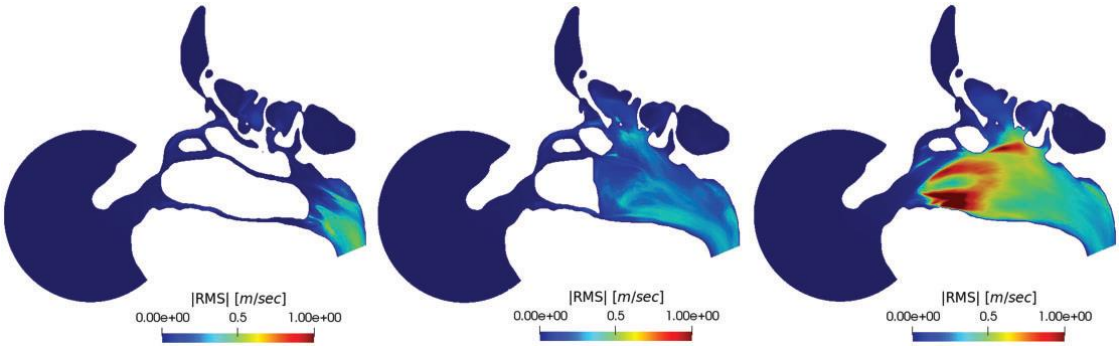

Figure 11 Root-mean-square (RMS) value of the fluctuations of the velocity magnitude in a sagittal plane. From left to right: baseline,, M-EMM, and EMM

In the M-EMM and EMM models, however, the velocity field shows significant fluctuations. The sites where the largest fluctuations are observed vary from M-EMM (where they are strongest just behind the IT stump) to EMM (where fluctuations are strongest in the former ethmoid/middle turbinate region). The maximum RMS value is larger in the EMM model than in the M-EMM model. The magnitude of the vorticity vector is shown in Figure 20. It grows progressively from the baseline to the EMM model.

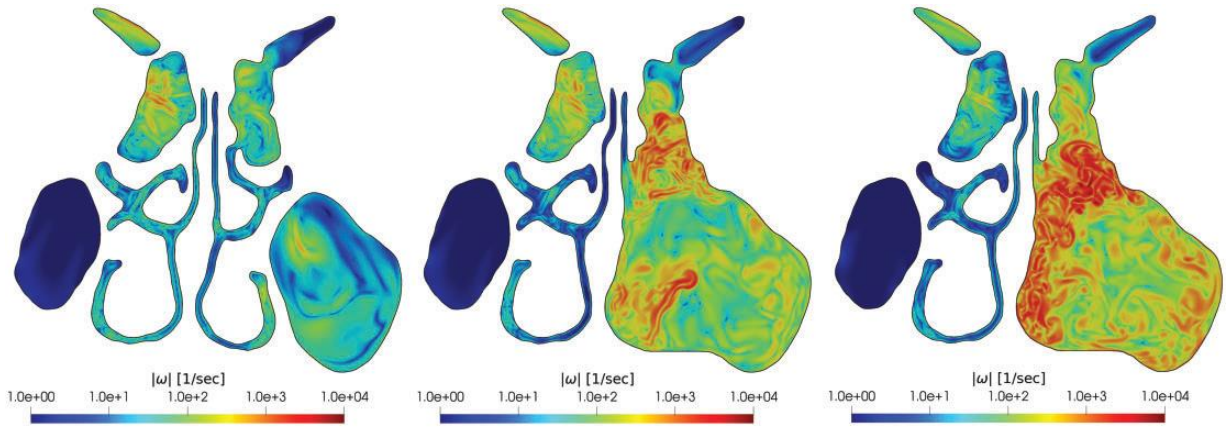

Figure 20 Magnitude of the instantaneous fluctuating vorticity vector in a coronal plane passing through the volume interested by surgery. Note the logarithmic color scale. From left to right: baseline, M-EMM, and EMM.

Vorticity is observed to progressively reach the lateral MS wall in the EMM model. M-EMM contains vorticity toward the midline, reducing MS involvement. Table 4 shows the volumetric average of the turbulent kinetic energy (K). Turbulence intensity increases by orders of magnitudes in the operated side and, less remarkably, in the M-EMM model.

	BASELINE	**M-EMM**	**EMM**
K VOLUME AVERAGE RIGHT (M_2/S_2)	0.000194	0.000301 (1.5x)	0.000845 (3.5x)
K VOLUME AVERAGE LEFT (M_2/S_2)	0.000165	0.006093 (35x)	0.028219 (170x)
K VOLUME AVERAGE TOT (M2/S2)	0.000359	0.006394 (16.8x)	0.029064 (79.9x)

Table 4: Abbreviations: EMM, endoscopic medial maxillectomy; M-EMM, modified endoscopic medial maxillectomy. The table reports the turbulent kinetic energy (K) volume average for the non-operated (right) side and the operated (left) side. The K volume average quantifies the increase of turbulence in the operated side; although with EMM the increase is by 170 times, with M-EMM the increase is only

Interestingly, the values show a definite, progressive increase through M-EMM to EMM also in the non-operated side. Figure 21 shows isosurfaces of the second eigenvalue λ2 of the velocity gradient tensor.

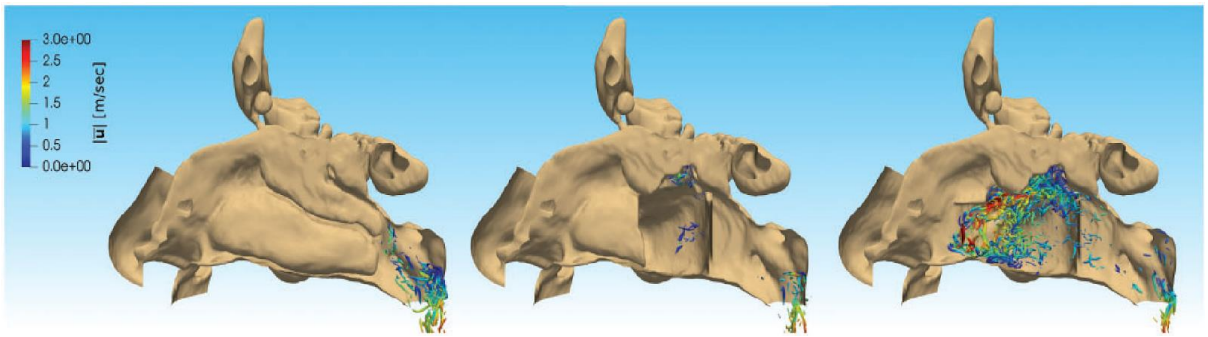

Figure 21 Isosurface of λ2= -650 000/s2 in an instantaneous velocity field, showing vortical structures, colored by the local value of the velocity vector. From left to right: baseline, M-EMM, and EMM.

This scalar quantity is used as a proxy to visualize turbulent vortical structures [63]; its spatial distribution does not provide indication of coherent large-scale vortices. It vividly illustrates how the flow is severely modified by EMM (and, to a much lesser extent, by M-EMM), where the large number of vortical structures correlates to the increased flow unsteadiness observed in Figures 18 and 19.

Discussion

The role of turbinates and lateral nasal wall in air conditioning has been studied and demonstrated with in silico and in vivo studies [91,94,95]. Similarly, the relationship between a failure in nasal conditioning and nasal crusting, especially after extensive surgery, has been thoroughly explored and demonstrated [96,97]. However, these speculations have been only marginally extended to the EMM. The disruption of normal nasal physiology in EMM is one of the main reasons why the more conservative M-EMM has been proposed [78,82]. However, to the authors' knowledge, only two CFD studies have explored the effects of EMM on the nasal function [89,90], providing insight into the change of flow patterns after EMM. Both are based on a single-patient analysis. Unfortunately, Qian et al.[89] used a simple mathematical approach, unable to provide information on the unsteady component of the flow, whereas in Lindemann the flow was driven by an extremely low pressure difference of only 1.3 Pa [89,90], times lower than the present study, implying a breathing intensity well below that at rest. In our work, a DNS based and time-resolved simulation is employed to assess unsteady phenomena at a physiological breathing rate. Even if an increase of the flow in the MS has already been thoroughly demonstrated after standard antrostomy procedures [98], our analysis finds EMM profoundly modify how the flow rate is partitioned between the two nasal airways. A certain amount of unbalance is physiological [6] : Indeed, in our baseline case, 42% of the flow rate pertains to the right passageway and 58% to the left. Within the specific constraint of a comparison carried out for the same global pressure drop, EMM determines a massive (+72%) relative increase of the flow rate on the operated side, with a significant reduction in the contralateral side too. Overall, the flow rate for the same pressure drop increases by 16.5%. On the other hand, M-EMM increases flow rate in the operated side much less dramatically, with minimal contralateral changes. The end result is a nearly equilateral flow rate distribution

(49% on the right side, 51% on the left), with only a 6.8% increase. Some studies indicated nasal cavity volume as the main predictive factor for air conditioning function, together with temperature distribution along the nasal surface [99]. Even in this respect, M-EMM scores better than EMM, although the significance of comparisons based on a constant pressure drop remains to be assessed. On the basis of this observation, it can be surmised that one of the main reasons for increased crusting, bleeding, and mucosal drying could be the direct effect of the airflow imbalance, influencing both the healthy and operated sides. This hypothesis might also explain why temporary postoperative changes affect the unmodified contralateral side. Our study finds that the topology of the flow field remains generally unchanged, with the sole difference that more streamlines reach the MS as the IT resection is increased. These findings are partially in contrast with data reported by Lindemann at much lower velocities [90]. Indeed, we have found that air still flows freely toward the nasopharynx in both the unaffected and operated sides, both in the EMM and M-EMM models.

Lindemann and colleagues [90] showed instead (albeit at low breathing intensity) large vortical structures disrupting the normal flow in the nasal cavities. Such structures have similarities with the vortices induced by radical turbinectomy in the solid model proposed by Perez-Mota et al. [92]. According to their findings, such vortices prevented the correct flow toward the nasopharynx, containing the air flow inside the operated nasal cavity. Indeed, instantaneous vorticity shown in Figures 20 and 21 points to the existence of small-scale vortical structures and does not contain evidence for large-scale coherent motions. Thanks to our DNS approach, the analysis based on the instantaneous fields has provided interesting insights into the pathophysiology of radical sinus surgery. The velocity field obviously reflects the flow rate changes and additionally provides spatial detail. As shown in Figures 15 and 16, the highest velocity is observed in an untreated patient along the middle meatus. In the EMM model, the

velocity in the contralateral side decreases, together with the flow rate, and higher velocities are observed in the lateral and cranial portions of the MS. This may decrease the effectiveness of the nose air conditioning effect in terms of humidification and warming. M-EMM reduces these effects, leaving the untreated side entirely unaffected and does not induce any velocity changes inside the MS. The analysis of the flow unsteadiness, only possible with a DNS simulation, is carried out for the first time in the context of maxillectomy and leads to a most interesting observation. The RMS value of the fluctuations of the velocity grows by an order of magnitude from the untreated model (where it is nearly negligible, in a steady laminar flow) to the maxillectomy models. The increase of the turbulent kinetic energy (K) volume integral, patently higher in both sides in the EMM model than in the M-EMM model, further confirms the increase of turbulence after surgery. Looking at Figures 18 and 19, the largest fluctuations are located in the former ethmoid/middle turbinate region, and Figure 21 relates them to small-scale vortical structures present in the flow. In our experience, but also in some cases series [77,84], this is also the location where most early postoperative crusting occurs. Therefore, our hypothesis is that a highly fluctuating flow field may induce local crusting due to the large and fluctuating shear stress. In the M-EMM model, the maximum of the fluctuations is found just behind the IT stump, far from mucosal boundaries. M-EMM could therefore reduce crusting—indeed often a temporary issue in EMM—by diverting large-scale highly oscillating flow structures from the mucosa. It would be interesting to further investigate how high velocity fluctuations and shear stress are connected with crusting in other sinonasal surgical procedures. Our analysis last focused on vorticity. As already shown in Figure 21, in the baseline model, the vorticity in the MS is negligible. Vorticity values progressively grow toward the lateral portion of the MS from the M-EMM model to the EMM model. While M-EMM contains disruptions toward the midline, EMM sees intense vorticity fluctuations near the

inferior and lateral MS walls. It is interesting to observe that the scarring and partial progressive concentric cavity closure that usually follow EMM occurs from those walls, where we might suppose a contribution from shear stress in scar tissues formation. Furthering our speculations, the formation of scar tissue induced by wall shear stress could also induce postsurgical nasal cavity remodeling, which would progressively lead to crusting and scabbing reduction thanks both to a more favorable geometry and higher tissue resilience. These observations are consistent with other studies on the postoperative MS, which showed in vivo how a higher wall shear stress correlates with residual crusting and discomfort [100].

Conclusion

The present data, though based on a single-patient analysis, shed light on the fluid dynamics that characterize radical sinus surgeries. In light of our findings, trans-nasal endoscopic partial maxillectomy types 1 and 2 have a theoretical CFD basis for their lower functional complication rate [101]. The computational cost prevents us from currently providing a dynamic model integrating different types of turbinate resections. Undoubtedly, such a model could help understand nuanced variation in nasal airflow, help tailor the turbinate resection, and provide the best surgical field visualization with the slightest fluid dynamics alteration. However, high-fidelity computational models addressing three radically different anatomical settings (two of which consist of commonly employed surgical techniques for EMM) facilitate understanding the changes in fluid dynamics in the nasal cavity. Our work is obviously limited in as much as it considers a single anatomy. Hence, its results cannot be immediately generalized, although much care was devoted to identifying a subject whose baseline anatomy is devoid of morphologic alterations and nasal symptoms as representative of a normal nose. However, our innovative computational approach uniquely provides access to information free from modeling error, and includes time dependency. Despite such limitations, the limited statistical significance of the study is in our opinion more than balanced by the availability of new and quantitatively reliable information.

7. Discussion and conclusion

In the previous chapters, three examples of the practical applications of CFD in nasal airflow research were presented. In every instance, the models were generated from actual CT scans, preventing simplifications of the nose's volumes and surfaces. Obviously, this option increases calculation complexity in exchange for better results.

In the first chapter, it was demonstrated how CFD can evaluate the diverse distributions of air flow in the nasal canals, enabling an accurate and timely examination of droplet dispersion. No other technology currently available permits such a comprehensive study. Moreover, because it is possible to impose a priori various flow properties, such as pressure, air temperature, flow speed, etc., even on the same model, there are numerous conditions that can be evaluated. In our study, we focused on the distribution of molecules as virus carriers and infection; however, the same model could be used to examine the distribution of droplets from nasal sprays or thermal water in the nasal fossa, as was done in a recently published paper by Buijs et al. [36], Sundström E et al .[102] and Kolanjiyil AV et al. [103]. The first group demonstrated that water droplet deposition patterns favor the middle meatus region over the inferior meatus region, with particle size and breathing intensity effects. The second and third experiments revealed that the nasal dispersion of two sprays with different droplet sizes was drastically different. Our investigation revealed that the deposition of the olfactory mucosa, which is believed to be a potential entry point for the virus into the central nervous system, is less likely during inhalation than during expiration. Therefore, CNS access should not be considered concomitant with the infection, but rather as a complication. It therefore suggests that local therapies aimed at enhancing the defense mechanisms of the olfactory mucosa may have a more robust protective mechanism than was previously believed.

The second and third chapters are devoted to surgical CFD applications. The availability of virtual models enables the insertion of various modifications, simulating virtually any type of nasal surgery and the resulting changes in nasal flow. In the second chapter, we simulated several types of turbinoplasty in order to determine how even minor modifications can significantly affect nasal airflow. As demonstrated in chapter three using a model of a medial maxillectomy, the more aggressive the surgery, the greater the consequences. On the other hand, the research presented here conveys a different message: not only can we investigate the effects of surgery, but we can also predict and prevent unintended consequences. The reported findings indicate that simple preservation of the head of the lower turbinates mitigates significantly the flow changes caused by treatments to the lateral nasal wall. In the near future, we anticipate a reduction in the informatic requirements of these programs, as well as the time required to obtain the models, thereby facilitating the tool's wider distribution and application. In the future, it may be possible to conduct simulations in near-real-time, allowing for a more thorough patient examination and more efficient surgical planning. Choosing the appropriate models is obviously required for information gathering. Unprecedented in the otolaryngological literature, chapter two presents a comparison between the RANS and DNS models. Significant percentage differences between the outcomes of the two methods are revealed by the obtained data, which is of great interest. This result is predictable, given that RANS provides mean values and subsequent errors, whereas DNS does not. We do not intend to disparage the RANS method a priori; however, it is not the most precise method we have access to. However, it has significantly lower economic and execution time expenses. Some hybrid approaches between RANS, LES, and DNS [104,105] have been studied in the engineering field in an effort to develop a more precise, yet equally sustainable method. In the near future, their potential medicinal uses must be

investigated. As previously stated, another essential characteristic for making CFDs usable and pervasive in the near future is their usability, which indicates the complete automation of operations through the use of artificial intelligence systems. This pathway demonstrates the OpenNose Project's value as a source and repository for clinical, radiological, and CFD data that can be used to create new simulations, projects, and informatics applications.

8. References

1. Pessey, J. J., Reitz, C. & Los, F. [Acute rhinosinusitis in the adult: national survey of general practice management]. *Rev Laryngol Otol Rhinol (Bord)* **121**, 237–241 (2000).
2. Ferrand, P. A. *et al.* [Acute sinusitus in adults. Management by general practitioners]. *Presse Med* **30**, 1049–1054 (2001).
3. Haapaniemi, J. J., Suonpää, J. T., Salmivalli, A. J. & Tuominen, J. Prevalence of septal deviations in school-aged children. *Rhinology* **33**, 1–3 (1995).
4. Smith, K. D., Edwards, P. C., Saini, T. S. & Norton, N. S. The prevalence of concha bullosa and nasal septal deviation and their relationship to maxillary sinusitis by volumetric tomography. *Int J Dent* **2010**, 404982 (2010).
5. Patel, R. Nasal Anatomy and Function. *Facial plast Surg* **33**, 003–008 (2017).
6. Kahana-Zweig, R. *et al.* Measuring and Characterizing the Human Nasal Cycle. *PLoS ONE* **11**, e0162918 (2016).
7. Hsu, D. W. & Suh, J. D. Anatomy and Physiology of Nasal Obstruction. *Otolaryngologic Clinics of North America* **51**, 853–865 (2018).
8. Sclafani, A. P., Gregory, J. K. & Achkar, J. *Total Otolaryngology-Head and Neck Surgery.* (Thieme Medical Publishers Inc).
9. Pignataro, L., Cesarani, A. & Felisati, G. *Trattato Di Otorinolaringoiatria Ed Audiologia*. (Edises, 2012).
10. Sainio, S., Blomgren, K. & Lundberg, M. Complications and number of follow-up visits after using septal stapler in septoplasty. *Rhin* **0**, (2019).
11. Gill, A. S., Said, M., Tollefson, T. T. & Steele, T. O. Update on empty nose syndrome: disease mechanisms, diagnostic tools, and treatment strategies. *Current Opinion in Otolaryngology & Head & Neck Surgery* **27**, 237–242 (2019).
12. Shah, K., Guarderas, J. & Krishnaswamy, G. Empty nose syndrome and atrophic rhinitis. *Annals of Allergy, Asthma & Immunology* **117**, 217–220 (2016).
13. Lee, T.-J. *et al.* Evaluation of depression and anxiety in empty nose syndrome after surgical treatment: Psychological Changes for ENS. *The Laryngoscope* **126**, 1284–1289 (2016).

14. Lemogne, C., Consoli, S. M., Limosin, F. & Bonfils, P. Treating empty nose syndrome as a somatic symptom disorder. *General Hospital Psychiatry* **37**, 273.e9-273.e10 (2015).

15. Clements, P. A. & Gortds, F. Standardisation Committee on Objective Assessment of the Nasal Airway, IRS, and ERS Consensus report on acoustic rhinometry and rhinomanometry. *Rhynology* **43**, 169–179 (2005).

16. Clement, P. a. R., Gordts, F., & Standardisation Committee on Objective Assessment of the Nasal Airway, IRS, and ERS. Consensus report on acoustic rhinometry and rhinomanometry. *Rhinology* **43**, 169–179 (2005).

17. Fokkens, W. J. *et al.* European Position Paper on Rhinosinusitis and Nasal Polyps 2020. *Rhinology* **58**, 1–464 (2020).

18. Thulesius, H. L., Cervin, A. & Jessen, M. Can we always trust rhinomanometry? *Rhin* **49**, 46–52 (2011).

19. Marambaia, P. P. *et al.* Can we use the questionnaire SNOT-22 as a predictor for the indication of surgical treatment in chronic rhinosinusitis? *Brazilian Journal of Otorhinolaryngology* **83**, 451–456 (2017).

20. Ferziger, J. H. & Perić, M. *Computational Methods for Fluid Dynamics*. (Springer Berlin Heidelberg, 2002). doi:10.1007/978-3-642-56026-2.

21. Pope, S. B. *Turbulent flows*. (Cambridge University Press, 2000).

22. Liu, Y., Matida, E., Gu, J. & Johnson, M. Numerical simulation of aerosol deposition in a 3-D human nasal cavity using RANS, RANS/EIM, and LES. *Journal of Aerosol Science* **38**, 683–700 (2007).

23. Matida, E. A., Finlay, W. H., Breuer, M. & Lange, C. F. Improving prediction of aerosol deposition in an idealized mouth using large-Eddy simulation. *J Aerosol Med* **19**, 290–300 (2006).

24. Mylavarapu, G. *et al.* Validation of computational fluid dynamics methodology used for human upper airway flow simulations. *J Biomech* **42**, 1553–1559 (2009).

25. Scialo, F. *et al.* ACE2: The Major Cell Entry Receptor for SARS-CoV-2. *Lung* **198**, 867–877 (2020).

26. Wan, D. *et al.* Neurological complications and infection mechanism of SARS-COV-2. *Signal Transduct Target Ther* **6**, 406 (2021).

27. Salian, V. S. *et al.* COVID-19 Transmission, Current Treatment, and Future Therapeutic Strategies. *Mol Pharm* **18**, 754–771 (2021).

28. Meinhardt, J. *et al.* Olfactory transmucosal SARS-CoV-2 invasion as a port of central nervous system entry in individuals with COVID-19. *Nat Neurosci* **24**, 168–175 (2021).

29. Bulfamante, G. *et al.* First ultrastructural autoptic findings of SARS -Cov-2 in olfactory pathways and brainstem. *Minerva Anestesiol* **86**, 678–679 (2020).

30. Perella, P., Tabarra, M., Hataysal, E., Pournasr, A. & Renfrew, I. Minimising exposure to droplet and aerosolised pathogens: a computational fluid dynamics study. *Br J Anaesth* **126**, 544–549 (2021).

31. Gupta, J. K., Lin, C.-H. & Chen, Q. Flow dynamics and characterization of a cough. *Indoor Air* **19**, 517–525 (2009).

32. Lechien, J. R. *et al.* Olfactory and gustatory dysfunctions as a clinical presentation of mild-to-moderate forms of the coronavirus disease (COVID-19): a multicenter European study. *Eur Arch Otorhinolaryngol* **277**, 2251–2261 (2020).

33. Giacomelli, A. *et al.* Self-reported Olfactory and Taste Disorders in Patients With Severe Acute Respiratory Coronavirus 2 Infection: A Cross-sectional Study. *Clin Infect Dis* **71**, 889–890 (2020).

34. 3D Slicer: A Platform for Subject-Specific Image Analysis, Visualization, and Clinical Support | SpringerLink. https://link.springer.com/chapter/10.1007/978-1-4614-7657-3_19.

35. Fedorov, A. *et al.* 3D Slicer as an Image Computing Platform for the Quantitative Imaging Network. *Magn Reson Imaging* **30**, 1323–1341 (2012).

36. Buijs, E. F. M. *et al.* Thermal water delivery in the nose: experimental results describing droplet deposition through computational fluid dynamics. *Acta Otorhinolaryngol Ital* **39**, 396–403 (2019).

37. Quadrio, M. *et al.* Effects of CT resolution and radiodensity threshold on the CFD evaluation of nasal airflow. *Med Biol Eng Comput* **54**, 411–419 (2016).

38. Balatinec, L., Uroić, T. & Jasak, H. Open-Source CFD Analysis of Nasal Flows. *OpenFOAM® Journal* **1**, 2–26 (2021).

39. Smagorinsky, J. General circulation experiments with the primitive equations: I. The basic experiment. *Monthly Weather Review* **91**, 99–164 (1963).

40. Crowe, C. T., Schwarzkopf, J. D., Sommerfeld, M. & Tsuji, Y. *Multiphase Flows with Droplets and Particles*. (CRC Press, 2011). doi:10.1201/b11103.

41. Hooper, R. G. Forced inspiratory nasal flow-volume curves: a simple test of nasal airflow. *Mayo Clin Proc* **76**, 990–994 (2001).

42. Braga, P. C. *et al.* Antioxidant effect of sulphurous thermal water on human neutrophil bursts: chemiluminescence evaluation. *Respiration* **75**, 193–201 (2008).

43. Hui, K. P. Y. *et al.* Tropism, replication competence, and innate immune responses of the coronavirus SARS-CoV-2 in human respiratory tract and conjunctiva: an analysis in ex-vivo and in-vitro cultures. *Lancet Respir Med* **8**, 687–695 (2020).

44. Hoffmann, M. *et al.* SARS-CoV-2 Cell Entry Depends on ACE2 and TMPRSS2 and Is Blocked by a Clinically Proven Protease Inhibitor. *Cell* **181**, 271-280.e8 (2020).

45. Zhao, K., Scherer, P. W., Hajiloo, S. A. & Dalton, P. Effect of Anatomy on Human Nasal Air Flow and Odorant Transport Patterns: Implications for Olfaction. *Chem Senses* **29**, 365–379 (2004).

46. Herbert, R. P. *et al.* Cytokines and olfactory bulb microglia in response to bacterial challenge in the compromised primary olfactory pathway. *J Neuroinflammation* **9**, 109 (2012).

47. Niazkar, H. R., Zibaee, B., Nasimi, A. & Bahri, N. The neurological manifestations of COVID-19: a review article. *Neurol Sci* **41**, 1667–1671 (2020).

48. Ahmad, I. & Rathore, F. A. Neurological manifestations and complications of COVID-19: A literature review. *J Clin Neurosci* **77**, 8–12 (2020).

49. Singh, S. *et al.* Nasopharyngeal wash in preventing and treating upper respiratory tract infections: Could it prevent COVID-19? *Lung India* **37**, 246–251 (2020).

50. Ramalingam, S., Graham, C., Dove, J., Morrice, L. & Sheikh, A. A pilot, open labelled, randomised controlled trial of hypertonic saline nasal irrigation and gargling for the common cold. *Sci Rep* **9**, 1015 (2019).

51. Pianta, L. *et al.* Acetic acid disinfection as a potential adjunctive therapy for non-severe COVID-19. *Eur Arch Otorhinolaryngol* **277**, 2921–2924 (2020).

52. Roithmann, R. Inferior turbinectomy: what is the best technique? *Braz J Otorhinolaryngol* **84**, 133–134 (2018).

53. Weber, R. K. & Hosemann, W. Comprehensive review on endonasal endoscopic sinus surgery. *GMS Curr Top Otorhinolaryngol Head Neck Surg* **14**, Doc08 (2015).

54. Balakin, B. V., Farbu, E. & Kosinski, P. Aerodynamic evaluation of the empty nose syndrome by means of computational fluid dynamics. *Comput Methods Biomech Biomed Engin* **20**, 1554–1561 (2017).

55. Malik, J. *et al.* Computational fluid dynamic analysis of aggressive turbinate reductions: is it a culprit of empty nose syndrome? *Int Forum Allergy Rhinol* **9**, 891–899 (2019).

56. Thamboo, A. *et al.* Defining surgical criteria for empty nose syndrome: Validation of the office-based cotton test and clinical interpretability of the validated Empty Nose Syndrome 6-Item Questionnaire. *Laryngoscope* **127**, 1746–1752 (2017).

57. Houser, S. M. Surgical treatment for empty nose syndrome. *Arch Otolaryngol Head Neck Surg* **133**, 858–863 (2007).

58. Li, C. *et al.* Computational fluid dynamics and trigeminal sensory examinations of empty nose syndrome patients. *Laryngoscope* **127**, E176–E184 (2017).

59. Li, C. *et al.* Investigation of the abnormal nasal aerodynamics and trigeminal functions among empty nose syndrome patients. *Int Forum Allergy Rhinol* **8**, 444–452 (2018).

60. Sozansky, J. & Houser, S. M. Pathophysiology of empty nose syndrome. *Laryngoscope* **125**, 70–74 (2015).

61. Hanida, S. *et al.* Examination of Extraction with Vortex Regions in Paranasal Sinus of Human Nose. in *6th World Congress of Biomechanics (WCB 2010). August 1-6, 2010 Singapore* (eds. Lim, C. T. & Goh, J. C. H.) 736–739 (Springer, 2010). doi:10.1007/978-3-642-14515-5_188.

62. Gerndt, A., Kuhlen, T., Van Reimersdahl, T., Haack, M. & Bischof, C. VR-based interactive CFD data comparison of flow fields in a human nasal cavity. *Proceedings of SPIE - The International Society for Optical Engineering* vol. 5367 65–76.

63. Jeong, J. & Hussain, F. Hussain, F.: On the identification of a vortex. JFM 285, 69-94. *Journal of Fluid Mechanics* **285**, 69–94 (1995).

64. Bates, A. Mechanics of airflow in human inhalation. (2014) doi:10.25560/25515.

65. Bates, A. J. *et al.* Dynamics of airflow in a short inhalation. *Journal of The Royal Society Interface* **12**, 20140880 (2015).

66. Zhao, K. & Jiang, J. What is normal nasal airflow? A computational study of 22 healthy adults. *Int Forum Allergy Rhinol* **4**, 435–446 (2014).

67. Menter, F. R. Two-equation eddy-viscosity turbulence models for engineering applications. *AIAA Journal* **32**, 1598–1605 (1994).

68. Lee, J. H., Na, Y., Kim, S. K. & Chung, S. K. Unsteady flow characteristics through a human nasal airway. *Respiratory Physiology and Neurobiology* vol. 172 136–146 (2010).

69. Chen, X. B., Lee, H. P., Chong, V. F. H. & Wang, D. Y. Impact of inferior turbinate hypertrophy on the aerodynamic pattern and physiological functions of the turbulent airflow - a CFD simulation model. *Rhinology* **48**, 163–168 (2010).

70. Lee, T. S., Goyal, P., Li, C. & Zhao, K. Computational fluid dynamics to evaluate the effectiveness of inferior turbinate reduction techniques to improve nasal airflow. *JAMA Facial Plastic Surgery* vol. 20 263–270 (2018).

71. Talmadge, J., Nayak, J. V., Yao, W. & Citardi, M. J. Management of Postsurgical Empty Nose Syndrome. *Facial Plast Surg Clin North Am* **27**, 465–475 (2019).

72. Tan, N. C.-W., Goggin, R., Psaltis, A. J. & Wormald, P.-J. Partial resection of the middle turbinate during endoscopic sinus surgery for chronic rhinosinusitis does not lead to an increased risk of empty nose syndrome: a cohort study of a tertiary practice. *Int Forum Allergy Rhinol* (2018) doi:10.1002/alr.22127.

73. Sindwani, R. Surgical treatment for empty nose syndrome. *Yearbook of Otolaryngology-Head and Neck Surgery* **2008**, 255 (2008).

74. Pinther, S., Deeb, R., Peterson, E. L., Standring, R. T. & Craig, J. R. Complications Are Rare From Middle Turbinate Resection: A Prospective Case Series. *Am J Rhinol Allergy* **33**, 657–664 (2019).

75. Covello, V., Pipolo, C., Saibene, A., Felisati, G. & Quadrio, M. Numerical simulation of thermal water delivery in the human nasal cavity. *Computers in Biology and Medicine* vol. 100 62–73 (2018).

76. Kamel, R. H. Transnasal endoscopic medial maxillectomy in inverted papilloma. *Laryngoscope* **105**, 847–853 (1995).

77. Erbek, S. S., Koycu, A. & Buyuklu, F. Endoscopic modified medial maxillectomy for treatment of inverted papilloma originating from the maxillary sinus. *J Craniofac Surg* **26**, e244-246 (2015).

78. Pagella, F., Pusateri, A., Giourgos, G., Tinelli, C. & Matti, E. Evolution in the treatment of sinonasal inverted papilloma: pedicle-oriented endoscopic surgery. *Am J Rhinol Allergy* **28**, 75–81 (2014).

79. Goudakos, J. K. *et al.* Endoscopic Resection of Sinonasal Inverted Papilloma: Systematic Review and Meta-Analysis. *Am J Rhinol Allergy* **32**, 167–174 (2018).

80. Busquets, J. M. & Hwang, P. H. Endoscopic resection of sinonasal inverted papilloma: a meta-analysis. *Otolaryngol Head Neck Surg* **134**, 476–482 (2006).

81. Bertazzoni, G. *et al.* Postoperative long-term morbidity of extended endoscopic maxillectomy for inverted papilloma. *Rhinology* **55**, 319–325 (2017).

82. Pagella, F. *et al.* 'TuNa-saving' endoscopic medial maxillectomy: a surgical technique for maxillary inverted papilloma. *Eur Arch Otorhinolaryngol* **274**, 2785–2791 (2017).

83. Ghosh, A., Pal, S., Srivastava, A. & Saha, S. Modification of endoscopic medial maxillectomy: a novel approach for inverted papilloma of the maxillary sinus. *J Laryngol Otol* **129**, 159–163 (2015).

84. Nakayama, T. *et al.* Endoscopic medial maxillectomy with preservation of inferior turbinate and nasolacrimal duct. *Am J Rhinol Allergy* **26**, 405–408 (2012).

85. Weber, R. K., Werner, J. A. & Hildenbrand, T. Endonasal endoscopic medial maxillectomy with preservation of the inferior turbinate. *Am J Rhinol Allergy* **24**, 132–135 (2010).

86. Chen, X. B., Lee, H. P., Chong, V. F. H. & Wang, D. Y. Numerical simulation of the effects of inferior turbinate surgery on nasal airway heating capacity. *American Journal of Rhinology and Allergy* vol. 24 e118–e122 (2010).

87. Chen, X. B., Lee, H. P., Chong, V. F. H. & Wang, D. Y. Aerodynamic characteristics inside the rhino-sinonasal cavity after functional endoscopic sinus surgery. *American Journal of Rhinology and Allergy* vol. 25 388–392 (2011).

88. Wang, F. *et al.* Management of maxillary sinus inverted papilloma via endoscopic partial medial maxillectomy with an inferior turbinate reversing approach. *Eur Arch Otorhinolaryngol* **274**, 4155–4159 (2017).

89. Qian, Y., Qian, H., Wu, Y. & Jiao, T. Numeric simulation of the upper airway structure and airflow dynamic characteristics after unilateral complete maxillary resection. *Int J Prosthodont* **26**, 268–271 (2013).

90. Lindemann, J. *et al.* Numerical simulation of intranasal airflow after radical sinus surgery. *Am J Otolaryngol* **26**, 175–180 (2005).

91. Hariri, B., Rhee, J. & Garcia, G. Identifying Patients Who May Benefit From Inferior Turbinate Reduction Using Computer Simulations. *Laryngoscope* vol. 125 2635–2641 (2015).

92. Pérez-Mota, J., Solorio-Ordaz, F. & Cervantes-de Gortari, J. Flow and air conditioning simulations of computer turbinectomized nose models. *Med Biol Eng Comput* **56**, 1899–1910 (2018).

93. Weller, H. G., Tabor, G., Jasak, H. & Fureby, C. A tensorial approach to computational continuum mechanics using object-oriented techniques. *Computers in Physics* **12**, 620–631 (1998).

94. Lindemann, J. *et al.* Temperature and humidity profile of the anterior nasal airways of patients with nasal septal perforation. *Rhinology* **39**, 202–206 (2001).

95. Keck, T., Leiacker, R., Heinrich, A., Kühnemann, S. & Rettinger, G. Humidity and temperature profile in the nasal cavity. *Rhinology* **38**, 167–171 (2000).

96. Garcia, G. J. M., Bailie, N., Martins, D. A. & Kimbell, J. S. Atrophic rhinitis: a CFD study of air conditioning in the nasal cavity. *Journal of Applied Physiology* **103**, 1082–1092 (2007).

97. Kastl, K. G., Rettinger, G. & Keck, T. The impact of nasal surgery on air-conditioning of the nasal airways. *Rhinology* **47**, 237–241 (2009).

98. Frank, D. O. *et al.* Quantification of airflow into the maxillary sinuses before and after functional endoscopic sinus surgery. *International Forum of Allergy and Rhinology* vol. 3 834–840 (2013).

99. Hanna, L. M. & Scherer, P. W. A Theoretical Model of Localized Heat and Water Vapor Transport in the Human Respiratory Tract. *Journal of Biomechanical Engineering* **108**, 19–27 (1986).

100. Choi, K. J., Jang, D. W., Ellison, M. D. & Frank-Ito, D. O. Characterizing airflow profile in the postoperative maxillary sinus by using computational fluid dynamics modeling: A pilot study. *American Journal of Rhinology and Allergy* vol. 30 29–36 (2016).

101. Turri-Zanoni, M. *et al.* Transnasal endoscopic partial maxillectomy: Operative nuances and proposal for a comprehensive classification system based on 1378 cases. *Head Neck* **39**, 754–766 (2017).

102. Sundström, E., Talat, R., Sedaghat, A. R., Khosla, S. & Oren, L. Computational Modeling of Nasal Drug Delivery Using Different Intranasal Corticosteroid Sprays for the Treatment of Eustachian Tube Dysfunction. *J Eng Sci Med Diagn Ther* **5**, 031103 (2022).

103. Kolanjiyil, A. V., Alfaifi, A., Aladwani, G., Golshahi, L. & Longest, W. Importance of Spray-Wall Interaction and Post-Deposition Liquid Motion in the Transport and Delivery of Pharmaceutical Nasal Sprays. *Pharmaceutics* **14**, 956 (2022).

104. Hattori, H., Umehara, T. & Nagano, Y. Comparative Study of DNS, LES and Hybrid LES/RANS of Turbulent Boundary Layer with Heat Transfer Over 2d Hill. *Flow Turbulence Combust* **90**, 491–510 (2013).

105. Voet, L. J. A., Ahlfeld, R., Gaymann, A., Laizet, S. & Montomoli, F. A hybrid approach combining DNS and RANS simulations to quantify uncertainties in turbulence modelling. *Applied Mathematical Modelling* **89**, 885–906 (2021).